

Article

# Effects of Urbanization and Seasonal Cycle on the Surface Urban Heat Island Patterns in the Coastal Growing Cities: A Case Study of Casablanca, Morocco

Hicham Bahi <sup>1,\*</sup>, Hassan Rhinane <sup>1</sup>, Ahmed Bensalmia <sup>1</sup>, Ute Fehrenbach <sup>2</sup> and Dieter Scherer <sup>2</sup>

<sup>1</sup> Faculty of Sciences Ain Chock, University Hassan II, Casablanca 20100, Morocco; h.rhinane@gmail.com (H.R.); a.bensalmia@get-maroc.ma (A.B.)

<sup>2</sup> Institute of Ecology, Technische Universität, Berlin 10623, Germany; ute.fehrenbach@tu-berlin.de (U.F.); dieter.scherer@tu-berlin.de (D.S.)

\* Correspondence: bahi.h88@gmail.com; Tel.: +212-662-787-752

Academic Editors: Benjamin Bechtel, Iphigenia Keramitsoglou, Simone Kotthaus, James A. Voogt, Klemen Zakšek, James Campbell, Richard Müller and Prasad S. Thenkabail

Received: 13 June 2016; Accepted: 24 September 2016; Published: 10 October 2016

**Abstract:** The urban heat island (UHI) phenomenon is a harmful environmental problem in urban areas affecting both climatic and ecological processes. This paper aims to highlight and monitor the spatial distribution of Surface UHI (SUHI) in the Casablanca region, Morocco, using remote sensing data. To achieve this goal, a time series of Landsat TM/ETM+/OLI-TIRS images was acquired from 1984 to 2016 and analyzed. In addition, nocturnal MODIS images acquired from 2005 to 2015 were used to evaluate the nighttime SUHI. In order to better analyze intense heat produced by urban core, SUHI intensity (SUHII) was computed by quantifying the difference of land surface temperature (LST) between urban and rural areas. The urban core SUHII appears more significant in winter seasons than during summer, while the pattern of SUHII becomes moderate during intermediate seasons. During winter, the average daytime SUHII gradually increased in the residential area of Casablanca and in some small peri-urban cities by more than 1 °C from 1984 to 2015. The industrial areas of the Casablanca region were affected by a significant rise in SUHII exceeding 15 °C in certain industrial localities. In contrast, daytime SUHII shows a reciprocal effect during summer with emergence of a heat island in rural areas and development of cool islands in urban and peri-urban areas. During nighttime, the SUHII remains positive in urban areas year-round with higher values in winter as compared to summer. The results point out that the seasonal cycle of daytime SUHII as observed in the Casablanca region is different from other mid-latitude cities, where the highest values are often observed in summer during the day.

**Keywords:** Landsat; MODIS; surface urban heat island; cool island; Casablanca; Morocco

## 1. Introduction

Since 1950, world urban population and urban infrastructure has grown rapidly [1]. Much research documented that this urban concentration leads to substantial climatological and meteorological problems [2], posing a heavy burden on the environmental sanitation and water quality, accompanied by a significant increase of air temperature [3–6]. The most important problem affecting urban microclimate is the urban heat island (UHI) that is considered as a difference of temperature between the urban and rural area [7]. The UHI results from several factors such as built-up intensity [8], city size [9], low albedo [4] and greenhouse gases emissions [10]. Its worsening is based on specific synoptic conditions which are summarized in anticyclonic weather, nebulosity and a low wind [11].

In addition to the adverse effects of heat islands on the local climate it affects human health [12,13] and contributes to excess mortality and morbidity [13–16]. In climatology, two types of UHI can be distinguished: the first one is called the atmospheric UHI, usually just called UHI, and is split into two subcategories: the urban canopy layer (UCL) heat island, and the urban boundary layer (UBL) heat island [17]. This first type can be assessed and studied by using meteorological data [18,19]. The second type is the surface UHI (SUHI), which can be assessed and studied by using land surface temperature (LST) data retrieved from thermal infrared satellite sensors [19,20]. The SUHI is controlled by surface heat fluxes and is substantially affected by urbanization [21]. It is based on remote sensing techniques and is a valid means to measure urban thermal environments [22], since spatial distribution of data acquired from weather stations do not reflect the spatial variation of temperatures caused by various land use/land cover (LULC) [21,23] especially in the built environment. Therefore, time series of satellite thermal observations allow us to better interpret processes and mechanisms of the SUHI associated with LULC change [24]. A variety of remote sensing products can be used to retrieve the LST such as Advanced Very High Resolution Radiometer (AVHRR) [9], Moderate-resolution Imaging Spectroradiometer (MODIS) [8,25–27], Advanced Spaceborne Thermal Emission and Reflection Radiometer (ASTER) [28–30], and Landsat [22,31,32]. Several models have been developed to quantify the correlation between LST and different parameters derived from remote sensing data, and to understand related spatial distributions. Indeed, models derived by statistical approaches were adopted to derive empirical relationships between LST and different socio-economic or biophysical factors such as population density [33], economic activity [34], land use and land cover [24,35], normalized difference vegetation index (NDVI) [10,36,37] and impervious surface abundance [38,39].

The SUHII was studied in different climatic zones and especially in the large metropolitan areas [28,40–42]. Furthermore, it can emerge due to land surface modification and anthropogenic heat emission in urban areas [43,44]. A study focused on quantifying the diurnal and seasonal SUHII in China's 32 major cities shows that SUHII differed considerably between day and night and varied greatly with season [45]. Some studies indicated that SUHII is more intense during the day than at night [39,46] and its intensity varies according to the climate conditions and geographical location of cities [45,47]. The seasonal variations of SUHII remains not well understood due to the several contrasting of the previous studies. Indeed, the SUHII in the major cities of China is still more pronounced in summer than in winter [45], while some of Japan's cities show that the spatial distribution of SUHII is weakest in summer and strong in winter [48].

Larger commercial cities of Morocco do not escape from the rules of rapid urbanization since they experienced significant social and economic changes over the last decades. Their attractiveness by national and foreign migrants is one of the essential factors explaining population growth [49]. The demographic increase in the region of Casablanca causes enough repercussion in a straightforward manner in the expansion of the built-up land and increasing need for more infrastructure at the expense of natural land. The city of Casablanca can therefore be expected to be exposed to intense UHI/SUHII [10]. Only one study focused on the evaluation of UHI pattern in the Casablanca region [10] but it does not describe its seasonal variation.

This study focuses on assessing and monitoring the spatial distribution of the surface urban heat island intensity from 1984 to 2015, in Casablanca region, in order to study the influence of season cycles and urbanization on SUHII patterns in Casablanca municipality and the cities at its outskirts and close by region.

This research is very promising and it is the first of its kind since it will enable us for the first time to have an overview about the seasonal variation and drivers of SUHII in the Casablanca region.

## 2. Study Area and Data

### 2.1. Study Area

The Casablanca region is located along the Atlantic coast, with a 50-km-long shore, in the center of Morocco. It covers the urban area of Casablanca and some of its surrounding cities and suburbs. The climate of the study area is characterized by Mediterranean and semi-arid climate with high oceanic influence. Its location along the Atlantic Ocean gives it soft and relatively wet winters and moderately warm summers without precipitation. The region is influenced by moderate air temperatures compared to other Moroccan and subtropical regions [50]. However, monthly mean air temperatures in Casablanca ranges from about 13 °C in January to 23 °C in August. In terms of precipitation, the annual rainfall is about 400 mm/year near the coast and about 300 mm/year in inland which usually occurs between the months of October and May [50]. The Casablanca region includes two prefectures (Mohammedia and Casablanca) and two provinces (Nouaceur and Mediouna), and spreads over an area of 1615 km<sup>2</sup> with a population of 4,270,750 inhabitants according to the 2014 census of September conducted by the High Commission for Planning (HCP), while population density exceeds 40,000 inhabitants/km<sup>2</sup> in some communes such as Al Fida and Ben M'sick (HCP). The region is bounded to the north, south and east by Chaouia-Ouardigha, and to the west by the Atlantic Ocean (Figure 1).

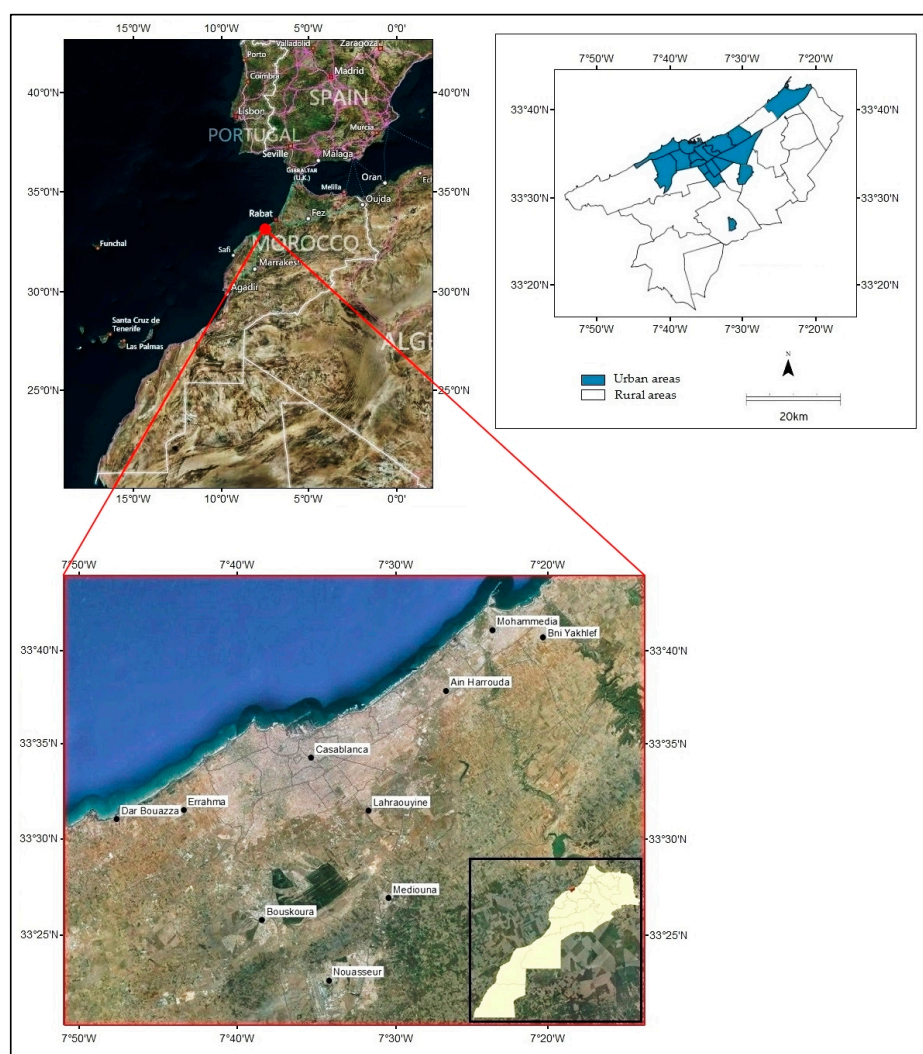


**Figure 1.** Study area showing Casablanca and its satellite cities.

## 2.2. Data Used

In this study, we used multi-temporal Landsat products acquired from the U.S. Geological Survey (USGS) from 1984 to 2016 (Table 1). Three Landsat products were employed in this study to compare seasonal and temporal differences in SUHI pattern, which are Landsat-5 Thematic Mapper (TM), Landsat-7 Enhanced Thematic Mapper (ETM+) and Landsat-8 Operational Land Imager/Thermal Infrared Sensor (OLI/TIRS).

**Table 1.** Landsat TM/ETM+/OLI-TIRS imagery used in this study.

Landsat Product	Acquisition Date	Path/Row	Spatial Resolution of TIR Band (m)	Id-Scene Information	Cycle
Landsat TM	25 August 1984	202/37	120	LT52020371984238XXX04	Daytime
Landsat TM	7 February 1987	202/37	120	LT52020371987038XXX08	Daytime
Landsat ETM+	8 February 2002	202/37	60	LE72020372002039EDC00	Daytime
Landsat TM	30 August 2003	202/37	120	LT52020372003242MTI01	Daytime
Landsat TM	10 November 2006	202/37	120	LT52020372006314MPS00	Daytime
Landsat TM	1 October 2009	202/37	120	LT52020372009274MPS00	Daytime
Landsat TM	8 January 2011	202/37	120	LT52020372011008MPS00	Daytime
Landsat TM	14 April 2011	202/37	120	LT52020372011104MPS00	Daytime
Landsat TM	8 November 2011	202/37	120	LT52020372011312MPS01	Daytime
Landsat OLI/TIRS	24 July 2013	202/37	100	LC82020372013205LGN00	Daytime
Landsat OLI/TIRS	6 April 2014	202/37	100	LC82020372014096LGN00	Daytime
Landsat OLI/TIRS	12 August 2014	202/37	100	LC82020372014224LGN00	Daytime
Landsat OLI/TIRS	3 January 2015	202/37	100	LC82020372015003LGN00	Daytime
Landsat OLI/TIRS	25 April 2015	202/37	100	LC82020372015115LGN00	Daytime
Landsat OLI/TIRS	17 June 2015	68/207	100	LC80682072015168LGN00	Nighttime
Landsat OLI/TIRS	6 January 2016	202/37	100	LC82020372016006LGN00	Daytime

Only Landsat image scenes covering the entire area of Casablanca region and without cloud cover were selected.

The OLI/TIRS was developed compared to the rest of Landsat sensors technology. Indeed, at the level of TIRS sensors and unlike for TM and ETM+ products, which have thermal infrared bands acquired in a single wavelength interval that ranges from 10.40 to 12.50  $\mu\text{m}$ , the Landsat 8 contains two thermal infrared bands similar to those of the MODIS thermal bands [51,52]. Thus, it is now possible to apply atmospheric correction of thermal imagery of Landsat-8 using the split-window techniques [51].

Since nocturnal Landsat images free of clouds were not available in our study area, except for the 17 June 2015, times series ranging between 2005 and 2015 were acquired from MODIS data (MOD11A2) in order to study the influence of season cycle on nocturnal SUHII. The MOD11A2 products (level 3) have a sinusoidal grid projection with a spatial resolution of 1 km, and represent the average values of the MOD11A1 data over eight days.

The MODIS LST were generated from two thermal infrared bands, 31 and 32, using the Split-Window algorithm. In this study, we look at the LST\_Night\_1 km local attribute of MOD11A2 products.

## 3. Methodology

Figure 2 summarizes the methodology adopted in this paper.

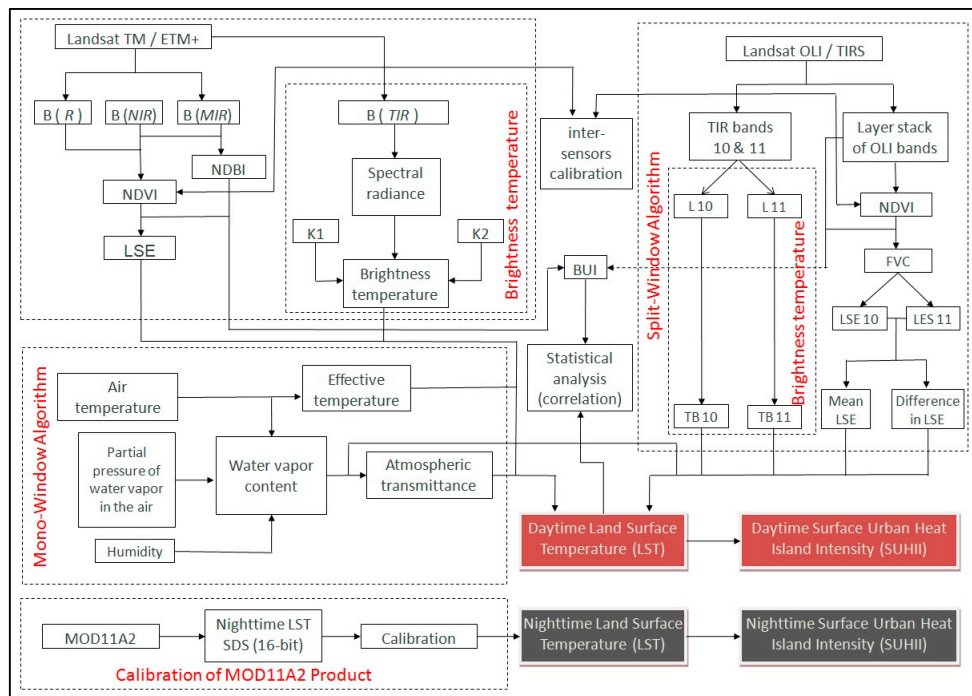


**Figure 2.** Flowchart of methodology (NDVI: normalized difference vegetation index; NDBI: normalized difference built-up index; K1 and K2: calibration constants; LSE: land surface emissivity; BUI: built up index; Li: spectral radiance of band I; FVC: fraction vegetation cover; TB: brightness temperature).

### 3.1. Data Preparation

Corrections were performed prior to processing and analyzing images. For the Landsat (TM/ETM+/OLI-TIRS) product, we converted the signals received by the sensors to TOA (Top Of Atmosphere) planetary reflectance [53–55]. Then, we combined this planetary reflectance with a correction of the solar elevation angle for more accurate reflectance calculations [55]. Processing of the thermal infrared bands was done by conversion digital numbers to spectral radiance.

Once the values of spectral radiance of the TM/ETM+/L8-TIRS thermal bands were computed, the brightness temperature, also called the effective at-satellite temperatures, can be calculated using the equation provided by the National Aeronautics and Space Administration. The conversion formula is given as Equation (1) [56].

$$T_b = \frac{K_2}{\ln(\frac{K_1}{L_\lambda} + 1)} \quad (1)$$

This transformation equation requires two calibration constants, which are listed in Table 2.

**Table 2.** Calibration constants used for effective at-satellite brightness temperature retrieval.

	Landsat 5 TM Band 6	Landsat 7 ETM+ Band 6	Landsat 8 TIRS	
			Band 10	Band 11
K1 [K]	607.76	666.09	774.89	480.89
K2 [W/(m <sup>2</sup> sr μm)]	1260.56	1282.71	1321.08	1201.14

### 3.2. Calculation of NDVI

The normalized difference vegetation index (NDVI) has been widely used as radiometric indicator for photosynthesis and hence vegetation cover [57] and density distribution of vegetation [58,59]. This index allows observing plant responses to climate change [60]. In this study, we used NDVI to determine the Land Surface Emissivity (LSE).

NDVI images of all scenes were obtained by calculating the ratio between the corrected reflectance of the red (R) and near-infrared (NIR) bands as mentioned in Equation (2) [61]:

$$\text{NDVI} = \frac{(\rho(\text{NIR}) - \rho(\text{R}))}{(\rho(\text{NIR}) + \rho(\text{R}))} \quad (2)$$

where  $\rho(\text{R})$  and  $\rho(\text{NIR})$  are the surface reflectance for the red bands and near-infrared bands, respectively.

### 3.3. Inter-Calibration of Data

Three Landsat products were used to retrieve LST. Several studies shows that the spectral bands of each product make relative gap (overlap) in term of spectral response compared to the similar bands used on other sensors [62–65]. These differences are more noticeable on the OLI Near InfraRed (NIR) band, which is narrower in order to eliminate the water vapor absorption effect at approximately 825 nm [52,63,64,66–68]. The relative spectral response differences may induce different values of at-sensor radiance while the sensors focus on a given region at the same time [64], and then at differences in reflectance values [52,63]. The Inter-sensor calibration (data normalization) method plays a key role in reducing reflectance differences of different sensors.

In this research, we statistically compared NDVI extracted from TM, ETM+ and OLI to improve its temporal continuity between different sensors. This method is considered as the most widely used in radiometric normalization of data. More than two hundred unchangeable pixels were used to study the inter-relationship between NDVI values, extracted from different sensors, according to seasons. The selected pixels show high inter-dependences between different dates with correlation coefficients ranging from 0.832 to 0.872 during winter, from 0.836 to 0.855 during autumn, from 0.946 to 0.957 during spring, and from 0.779 to 0.924 during summer (Figure 3). The inter-calibration processing was done by considering the OLI data as reference since its radiometric performance was improved compared to the previous Landsat products.

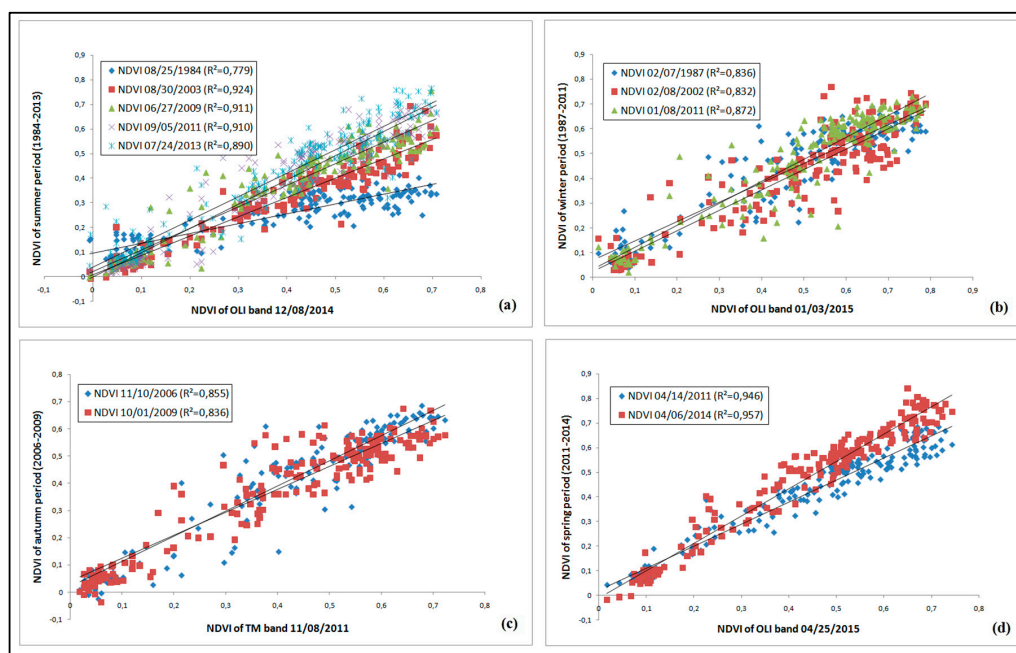


**Figure 3.** Inter-calibration of NDVI extracted from Landsat imageries according to the seasons: (a) summer inter-calibration of NDVI; (b) winter inter-calibration of NDVI; (c) autumn inter-calibration of NDVI; and (d) spring inter-calibration of NDVI.

### 3.4. Retrieval of LSE

The estimation of an accurate LST requires estimating emissivity. Many methods have been proposed and approved to derive the LSE from NDVI. Among the most used, one is that shown in Equation (3) [69–72], which is based on the relationship between emissivity in the thermal infrared and NDVI, and shows that the LSE varies according to the proportion of vegetation and bare soil.

$$\varepsilon = \begin{cases} a + b\text{pred} & \text{when NDVI} < 0.2 \\ \varepsilon_v P_v + \varepsilon_s (1 - P_v) + d\varepsilon & \text{when } 0.2 \leq \text{NDVI} \leq 0.5 \\ \varepsilon_v + d\varepsilon & \text{when NDVI} > 0.5 \end{cases} \quad (3)$$

where  $\varepsilon_v$  is the vegetation canopy emissivity,  $\varepsilon_s$  is the bare soil emissivity,  $d\varepsilon$  is the internal reflection emissivity due to cavity effect, this term equal to 0 in the case of homogenous surface [73], and  $P_v$  is the vegetation proportion achieved that can be estimated from  $\text{NDVI}_{\min}$  and  $\text{NDVI}_{\max}$  referring, respectively, to non-vegetated and fully vegetated land covers. The  $P_v$  term was calculated using the following equation [74]:

$$P_v = \left[ \frac{\text{NDVI} - \text{NDVI}_{\min}}{\text{NDVI}_{\max} - \text{NDVI}_{\min}} \right]^2 \quad (4)$$

This technique has been validated in different areas from mid-latitude to tropical and allows us to estimate emissivity with error of 0.6% [69]. This error is acceptable since any method for the emissivity determination should not exceed an error of 1.7% and half of these values when using the split-window algorithm [69].

### 3.5. Retrieval of Land Surface Temperature

LST is a key variable in earth environment research for evapotranspiration [75,76] and urban heat island monitoring [24,77–79]. Several algorithms have been developed to retrieve LST from satellite data, namely the Mono-Window algorithm [80], Single-Channel algorithm [81], Split-Window algorithm (Multi-Channel algorithm) [82,83], Dual-Angle algorithm [84], Multi-Angle algorithm [85–87], and the one described by Planck's law [88].

In this study, two algorithms were used to retrieve the LST from Landsat images, namely the Mono-Window and Split-Window algorithms. Mono-Window algorithm was used to derive the LST from band 6 of TM and ETM+ sensors. The expression of Mono-Window algorithm is as follows [80]:

$$T_s = \frac{a \times (1 - C - D) + (b \times (1 - C - D) + C + D) \times T_i - D \times T_a}{C} \quad (5)$$

where  $T_s$  is the land surface temperature (in K),  $T_i$  is the brightness temperature,  $T_a$  is the effective mean atmospheric temperature estimated from water vapor distribution in the atmospheric profile [89], and  $a$  and  $b$  are two constants equal, respectively, to  $-67.355351$  and  $0.458606$ .  $C$  and  $D$  are two parameters that can be calculated according to the emissivity and atmospheric transmittance, respectively.

Split-Window algorithm was used to estimate LST from Landsat 8, since it is the first Landsat series that incorporates two TIR bands in the atmospheric window between  $10\text{--}12\text{ }\mu\text{m}$ . The strength of this technique is that, in addition to emissivity, only one parameter is required, i.e., water vapor content. The Split-Window algorithm is expressed as follows:

$$T_s = T_{10} + c_1 \times (T_{10} - T_{11}) + c_2 \times (T_{10} - T_{11})^2 + c_0 + (c_3 + c_4 \times \omega) \times (1 - \varepsilon) + (c_5 + c_6 \times \omega) \times \Delta\varepsilon \quad (6)$$

where

$T_s$ : Land surface temperature in Kelvin;

$c_0$  to  $c_6$ : Split-Window coefficient [90];

$T_{10}$  and  $T_{11}$ : At-sensor brightness temperature at band 10 and 11;

$\varepsilon$ : Mean of land surface emissivity of band 10 and 11;

$\Delta\varepsilon$ : Difference between land surface emissivity of band 10 and band 11;  
 $\omega$ : Atmospheric water vapor content.

### 3.6. Calculation of SUHII

To better analyze areas affected by anthropogenic heat emissions, the SUHI intensity (SUHII) was computed as the difference between the pixel value of LST and the average LST of surrounding areas of the urban core (not including water bodies) [43] characterized by a low population, abundant vegetation and fallow land.

### 3.7. Calculation of Built-Up Land Information

In remote sensing, several indexes have been proposed for delineation of built-up land and for exploration of LU/LC types. One of the most important techniques for monitoring the distribution of urban areas is the Normalized Difference of Built-up Index (NDBI) [91], derived as:

$$\text{NDBI} = \frac{(\rho(\text{MIR}) - \rho(\text{NIR}))}{(\rho(\text{MIR}) + \rho(\text{NIR}))} \quad (7)$$

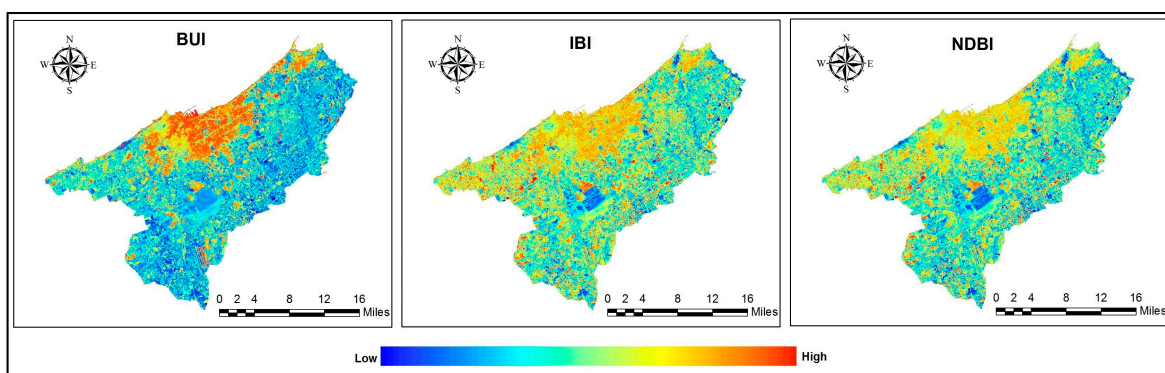
where MIR and NIR are the middle infrared and the near infrared band, respectively.

Another index, called Index-based Built-up Index (IBI), derived from existing indices, was proposed by Xu [92]. The three thematic indices used in developing the IBI index are the soil adjusted vegetation index (SAVI), the modified normalized difference water index (MNDWI) and the NDBI. The strength of this index is that it offers the possibility of eliminating background noise while retaining built-up land characteristics in satellite imagery [92].

Using NDBI and IBI confronts us with an issue of distinguishing built areas outside cities, since these two indices provide an important overlap between bare soil, fallow land and built-up areas. Therefore, the accuracy of these indices remains limited to urban areas. To address this overlap issue, we used a third one called Built Up Index (BUI), which is able to map built-up areas at an accuracy level of 92.6% [91], using the difference between NDBI and NDVI (Equation (8)).

$$\text{BUI} = \text{NDBI} - \text{NDVI} \quad (8)$$

Figure 4 shows the differences among NDBI, IBI and BUI.



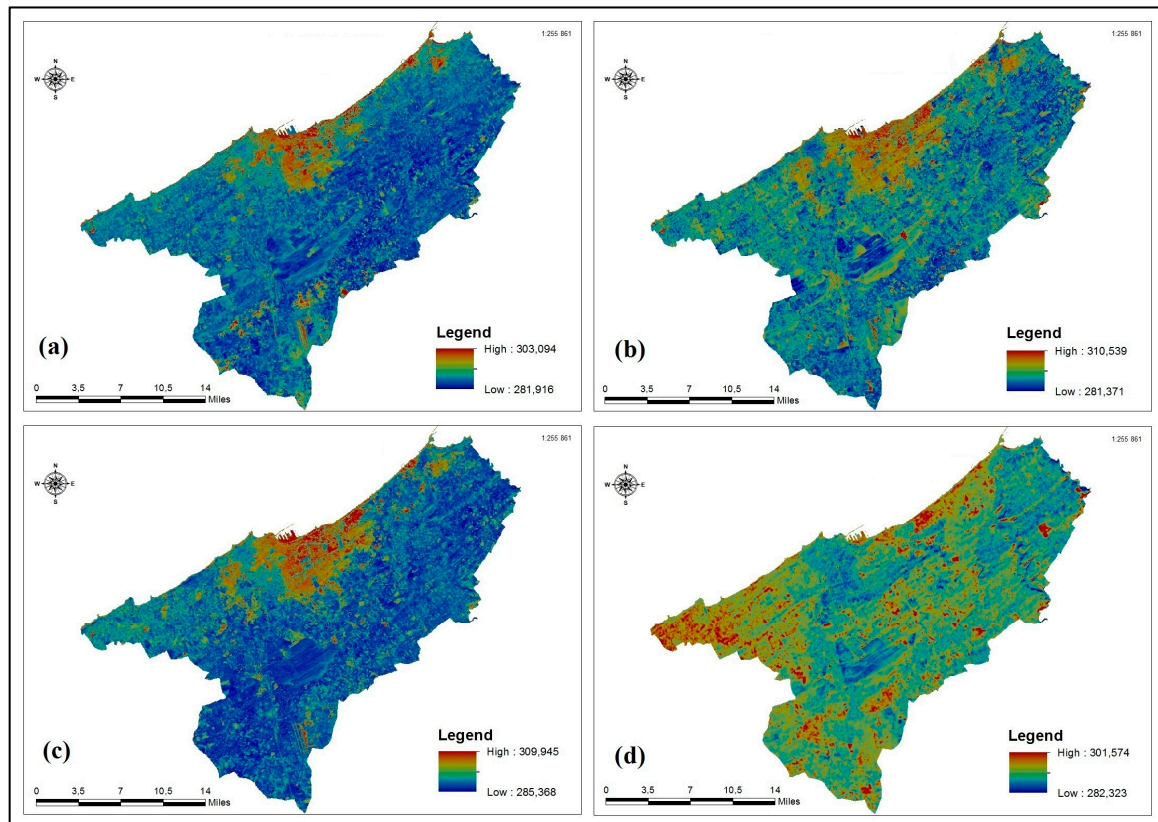
**Figure 4.** Extraction of buildings using BUI, IBI and NDBI.

Figure 4 demonstrates that BUI allow us to better delineate the urban areas and shows high values in the urban zone compared to the NDBI and IBI.

## 4. Results

### 4.1. Spatial Distribution of LST in Winter

Spatio-temporal variation of daytime SUHII for LST estimations during winter shows an important concordance between urban concentration and LST. This relationship is more significant in municipalities and region coinciding with important density of built up or industrial areas experiencing important air pollution emissions (Figure 5a–c). Land cover classifications have been established to show the dynamics of urban cores and vegetation at the study area between 1987 and 2015 (Figure 6).



**Figure 5.** Spatial distribution of LST during winter from 1987 to 2015: (a) LST retrieved from TM (7 February 1987); (b) LST retrieved from ETM+ (8 February 2002); (c) LST retrieved from TM (8 January 2011); and (d) LST retrieved from OLI/TIRS (3 January 2015).

The interpretation of the satellite images shows also that during winter the daytime SUHII in the urban area become more significant when air temperature exceeds the average winter temperature which ranges from 15 to 16.5 °C as shown in Figure 5a–c (with minimum air temperature of approximately 13 °C). The presence of low outdoor temperature contributes significantly to reducing soil moisture deficit [47,93,94], which is more sensitive to air temperature than precipitation [47], and hence to reducing the emergence of daytime SUHII in the permeable cover of urban core characterized by partial vegetation cover. The result illustrated in Figure 5d accentuates this effect and shows a weak SUHII in Casablanca region on 3 January 2015, since that day, and during the consecutive three previous days, the Casablanca region had air temperature below winter average temperature (average air temperature in the neighborhood of 11.5 °C with air temperature of approximately 6.4 °C at 8 am which correspond to the half of minimum temperature of Figure 5a–c). Preceding precipitations can also impact this phenomenon. We highlight in the discussion section that these urban cooling zone coincide exactly with areas affected by intense precipitations.

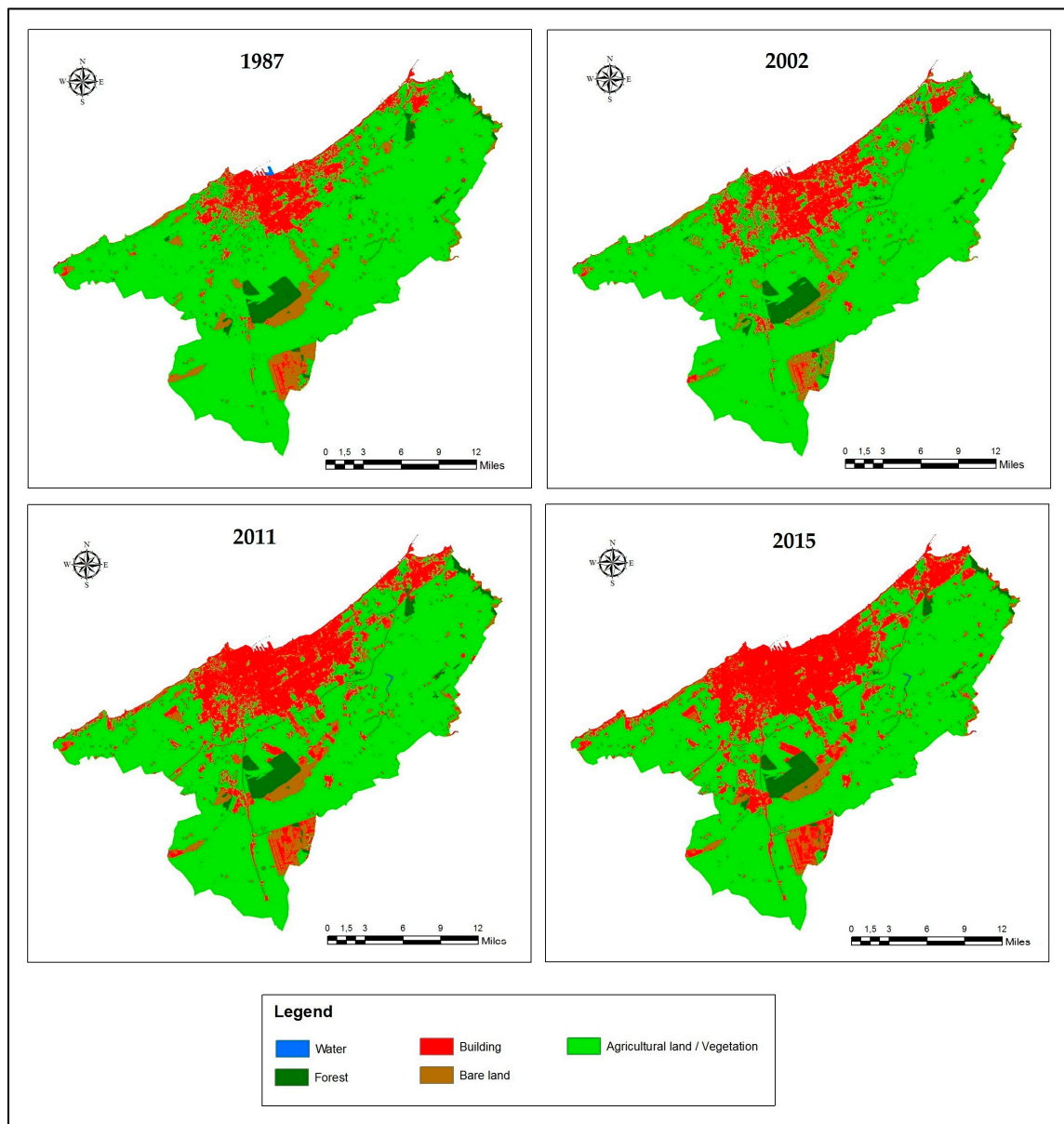


**Figure 6.** Land cover classification of Casablanca region from 1987 to 2015.

#### 4.2. Statistical Analysis Between LST and Urbanization in Winter

A statistical analysis correlating BUI and LST was performed. More than 2.5 million values referring to all pixels were used to study the concordance strength between these two quantities for each day. The results of the statistical analysis show a strong positive linear relationship between these two quantities when the air temperature exceed the average winter air temperature with coefficient correlation of approximately 0.85 (Figure 7a–c), while the strength of the link weakens on cooler days (correlation coefficient of 0.322) (Figure 7d).

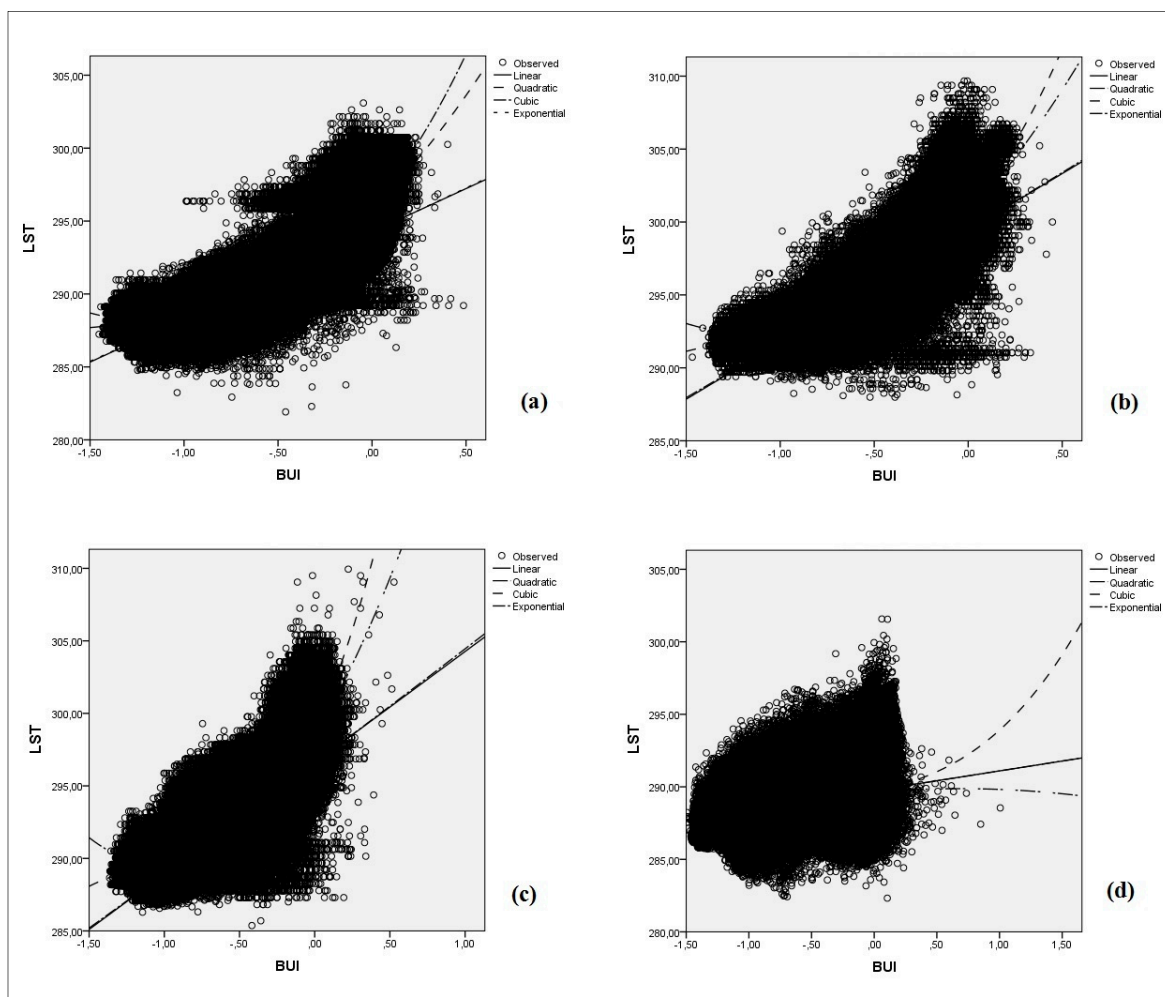


**Figure 7.** Correlation study between LST and BUI: (a) 7 February 1987 BUI/LST correlation study ( $R^2 = 0.847$ ); (b) 8 February 2002 BUI/LST correlation study ( $R^2 = 0.865$ ); (c) 8 January 2011 BUI/LST correlation study ( $R^2 = 0.849$ ); and (d) 3 January 2015 BUI/LST correlation study ( $R^2 = 0.322$ ).

#### 4.3. Evolution Analysis of SUHII in Winter

The data analysis shows that the daytime SUHII significantly increased between 1987 and 2011 in Casablanca city and some of neighboring small cities around the economic metropolis. Casablanca region daytime SUHII between 1987 and 2011 increased by  $1.34\text{ }^\circ\text{C}$ ,  $4.01\text{ }^\circ\text{C}$ ,  $4.27\text{ }^\circ\text{C}$  and  $0.67\text{ }^\circ\text{C}$  for Casablanca, Errahma, Lahraouyine and BniYekhlef, respectively (Figure 8).

During the winters from 1987 to 2011, maximum SUHII values increased substantially. Furthermore, we observed a significant surge of daytime SUHII in industrial and commercial areas with threshold that can reach  $18\text{ }^\circ\text{C}$  as compared to rural areas. Mohammedia and Casablanca industrial zones experienced significant release of air pollution, which contributed to raise SUHII values, since emissions from industries contribute significantly in enhancing global warming [95–98]. Winter SUHII can be used as an indicator of climate change since urbanization that contributes to  $\text{CO}_2$  emissions [99] and the highest SUHII values are marked in these areas and explain warming.

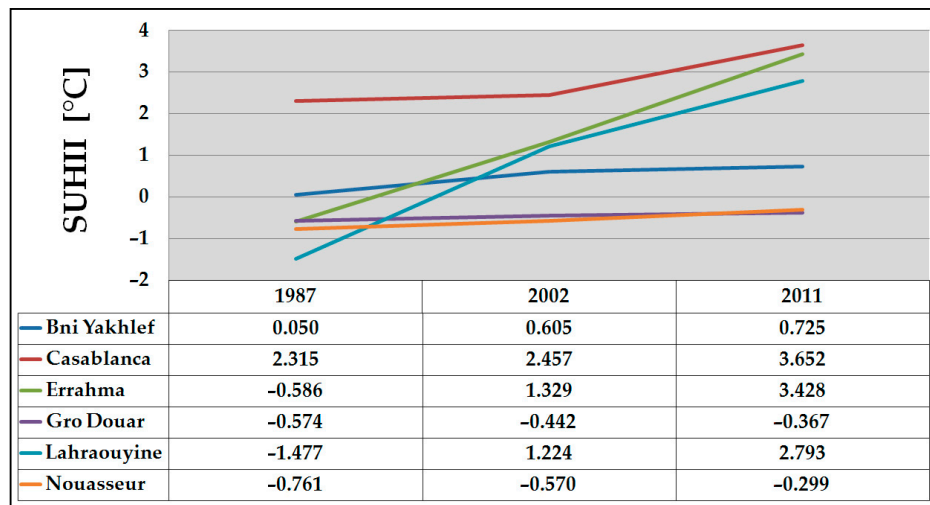


**Figure 8.** Variation of the average daytime SUHII during winter from 1987 to 2011 (obtained from average winter SUHII in 1987, 2002 and 2011).

The following graph (Figure 9) represents the variation of the maximum SUHII in the industrial area during winter from 1987 to 2011 calculated from maximum winter SUHII in 1987, 2002 and 2011.

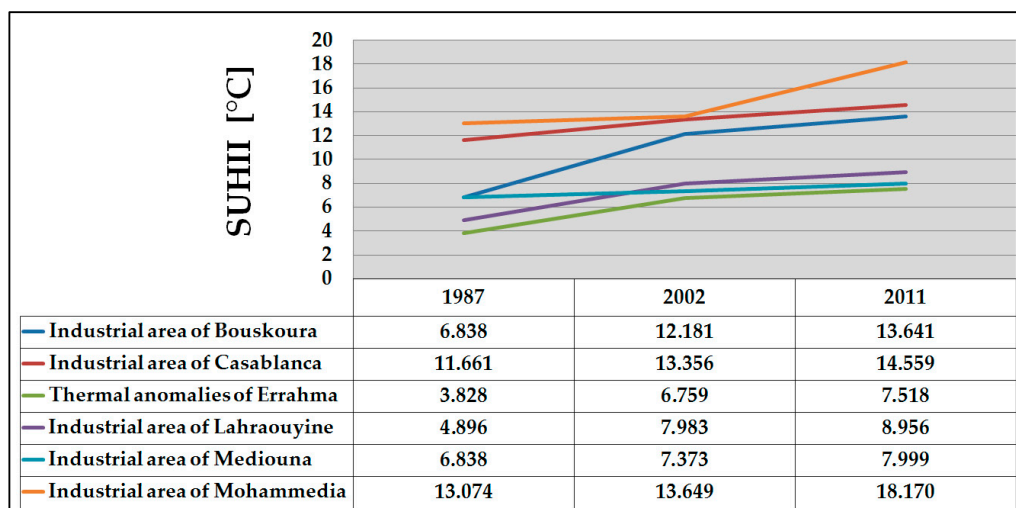


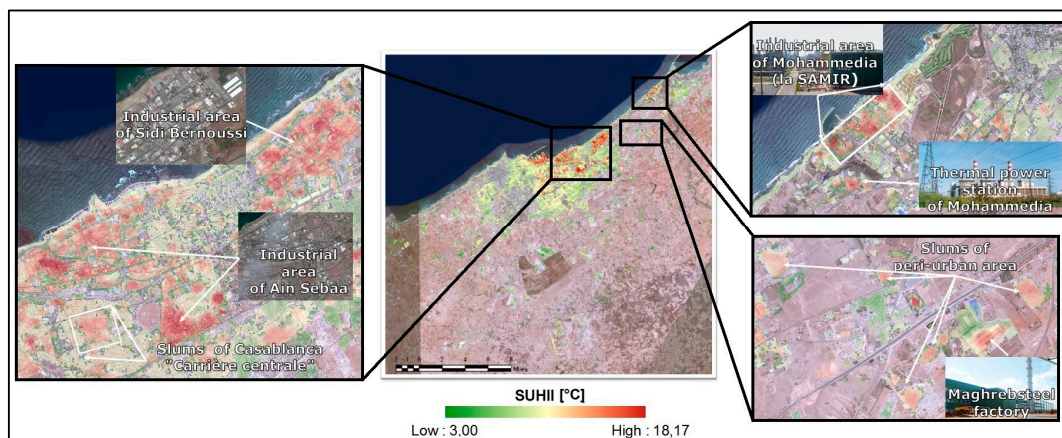
**Figure 9.** Variation of the maximum SUHII during winter from 1987 to 2011 (obtained from maximum winter SUHII in 1987, 2002 and 2011).

In order to better understand the intense anthropogenic heat pattern in the Casablanca region during winter, we proceeded a robust statistical method proposed in 2007 by Zhang [100], which brings more credibility compared to the conventional segmentation technique based on the arbitrary choice of the threshold value [100]. This method allows to divide the LST/SUHII into different scales and different times of standard deviation [100] (Equation (9)).

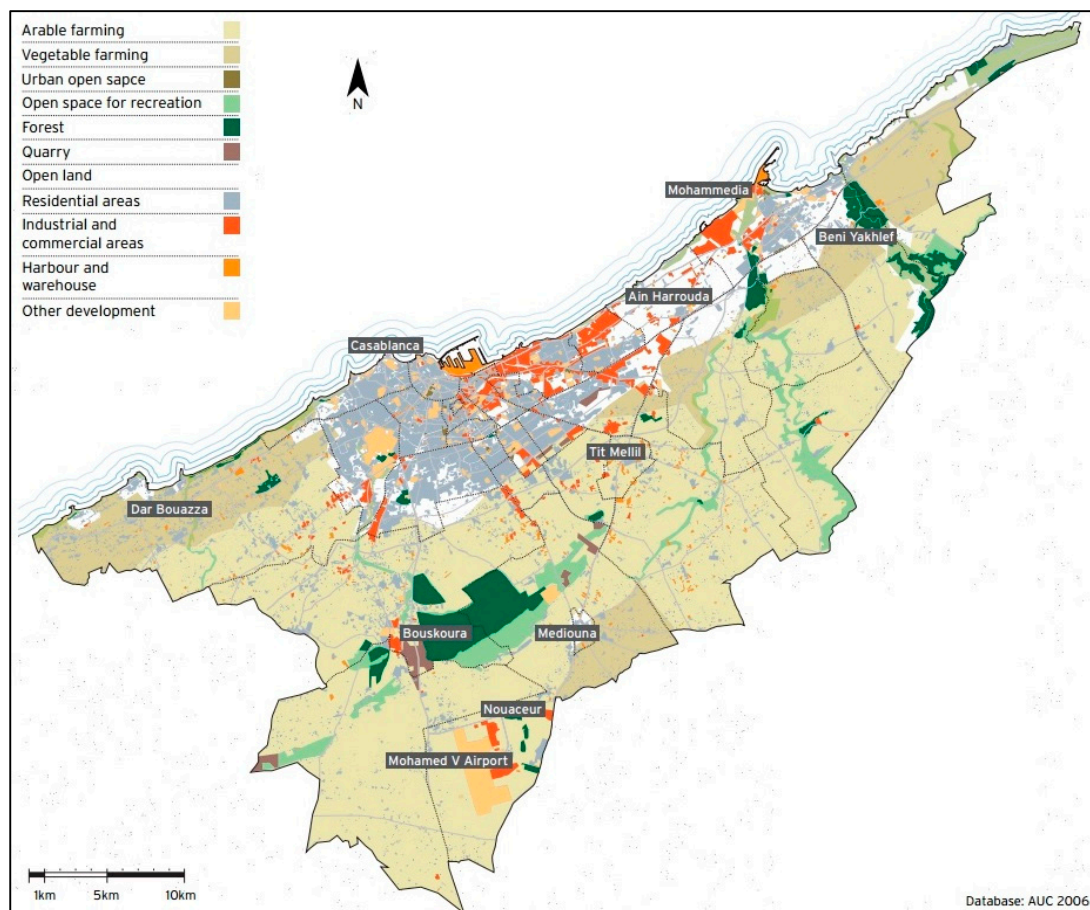
$$T = a \pm \chi \times s \quad (9)$$

where T is the SUHII partition boundary value; a is the average SUHII;  $\chi$  is the statistical series with step of 0.5; and s is standard deviation. The basis of this technique is to subdivide the SUHII into three classes: normal SUHII, low SUHII and high SUHII.

The result of the segmentation method (Figure 10) shows important emergence of SUHII in some urban areas and city outskirts in addition to the industrial zones identified previously. A significant increase of daytime SUHII in slums zone, buildings concentration, and elevated structure of buildings and parking lots was noticed. Table 3 shows the variation of daytime SUHII during winter of 2011 within areas exposed to intense anthropogenic heat, while Figure 11 shows the land use of Casablanca region. The highest SUHII was marked in industrial zone of Mohammedia and especially in factories specializing in the refining of petroleum products.



**Figure 10.** Spatial distribution of more intense SUHII within the Casablanca region.

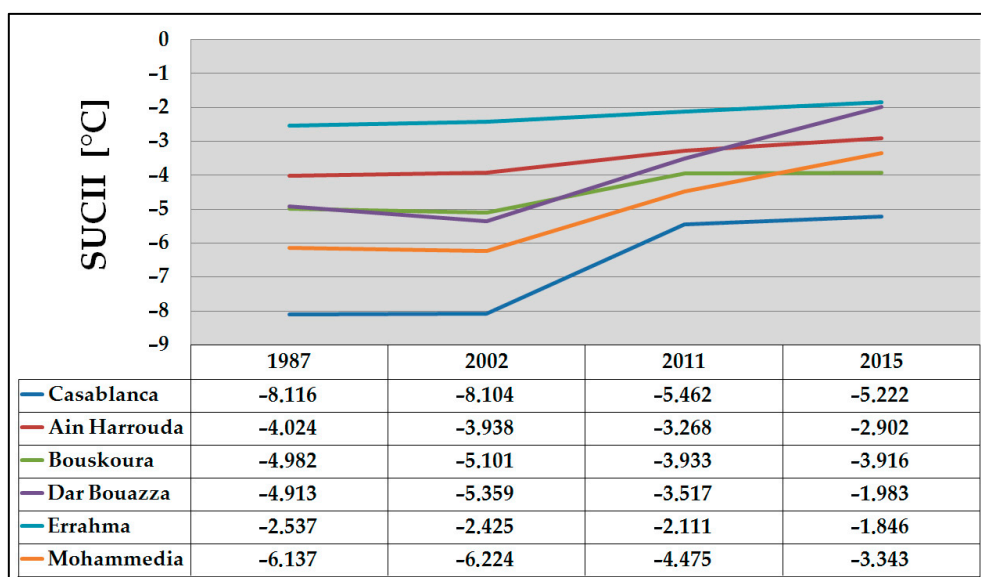


**Figure 11.** Land use of Casablanca region (Source: Urban Agency of Casablanca, 2006).

**Table 3.** Variation of daytime SUHII within areas exposed to intense anthropogenic heat.

Classes	Daytime SUHII Range (°C)	
	From	To
Tall building	-	7.51
Areas of high concentration (old city)	6.54	8.48
Slums	7.03	10.38
Commercial activity	4.61	9.91
Industrial areas	7.03	18.17

Although the period between 1 and 3 January 2015 was affected by low temperature, we observed substantial rising of minimum surface urban cool island intensity (SUCII) (negative SUHII) in green spaces during the winter period between 1987 and 2015 (Figure 12). This increasing is due mainly to the warming trends [12] and important expansion of the city at the expense of the green space and farmland (land use/land cover change) [12].

**Figure 12.** Variation of minimum winter SUHII (°C) from 1987 to 2015 (obtained from winter SUHII in 1987, 2002, 2011 and 2015).

The recent urban development of Mohammedia towards the North enhanced this effect. Urban development also occurred in Bouskoura and Errahma, which experienced massive construction encroaching over farmland.

Built environment encroaching over natural surfaces plays a key role in the loss of humidity and water available for vegetation, reducing evaporation rates. On the other hand, the thermal properties of different materials used in the construction greatly affect the urban heat island phenomenon. The roads and the roof of urban areas are usually paved with black asphalt and other materials that have low solar reflectance. The energy of the sunlight is converted into thermal energy [100], which explains why these materials capture the heat when exposed to the solar radiation. Poor governance of urban development is expected to lead to significant increase in SUHII and a reduction in the potential cooling effect provided by vegetation.

Urban development encroaching over farmland affects also food security. However, higher temperatures may also impact water availability and hence crop production [101,102]. Warmer urban environment also affects temperature-related morbidity of urban dwellers [12,103,104]. Hence, with a difference in winter SUHII between industrial areas and the remaining regions of Casablanca that can exceed 18 °C, people employed in factories and living nearby these areas are especially vulnerable.

#### 4.4. Spatio-Temporal Evolution of SUHII in Summer

During summer, the spatial distribution of daytime SUHII faces a reciprocal effect with the emergence of more intense surface heat island on fallow lands and harvested fields (Figure 13). Results show a substantial increase of cool islands in urban and peri-urban zones, and allow better demarcation of urban areas. However, a visual interpretation of images (Figure 13) shows that during 1984–2014 the Casablanca metropolis underwent dramatic change of urban area at the expense of farmland. The industrial areas remain relatively affected by significant SUHII ranging from 2 to 7 °C.

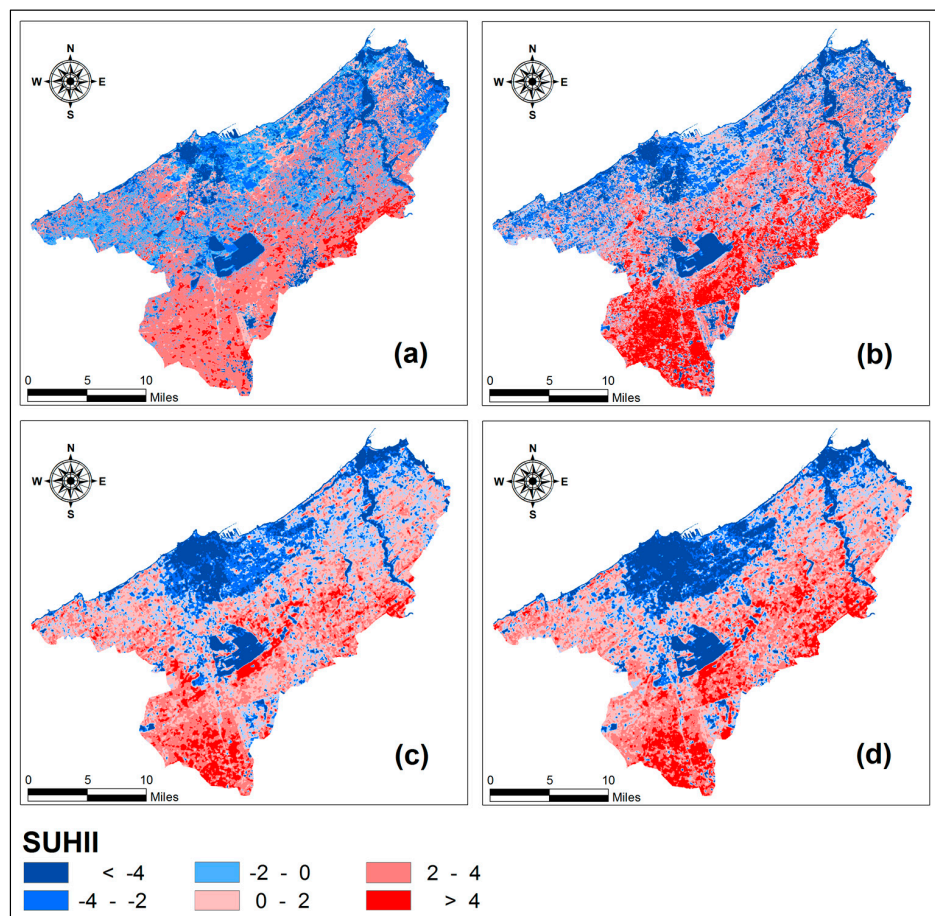


**Figure 13.** Variation of daytime SUHII during the summer periods between 1984 and 2014: (a) SUHII of 25 August 1984 retrieved from TM; (b) SUHII of 30 August 2003 retrieved from TM; (c) SUHII of 24 June 2013 retrieved from OLI/TIRS; and (d) SUHII of 12 August 2014 retrieved from OLI/TIRS.

The presence of cool islands in the city was reported in several urban climate studies [50]. However, a recent study analyzed UHI and their characteristics, in Asian and Australian cities and regions shows an important emergence of daytime cool islands in some cities [105]. Cooler areas were observed in four Asian cities (Beijing, Kuala Lumpur, Seoul and Singapore), and two Australian cities (Adelaide and Melbourne) [105]. The same results were found in few cities surrounded by desert, such as Jeddah in Saudi-Arabia and Mosul in Iraq [46].

The existence of urban cool islands in the Casablanca region during summer is certainly due to its geographical location at the coast. However, the presence of the sea breeze during the daytime of warm periods allows the transfer of the relatively cooler air into the city and enhances wind speeds [105,106]. Hence, the sea breeze contributes significantly in reducing heat island intensity in coastal cities. This cooling effect from the sea breeze declines with distance from the coast [48,107]. The shading caused by tall buildings may also induce development of cool island areas [108].

#### 4.5. SUHII Pattern in Autumn and Spring Period

During autumn and spring, the spatial distribution of daytime SUHII becomes unstable (Figure 14). Therefore, the spatial pattern of daytime SUHII shows a transitional phase with shifting of surface heat island intensity from the rural to the urban area and vice versa, while we observe an important surface heat island intensity in the industrial areas, bare land and farmland in biological recovery periods.

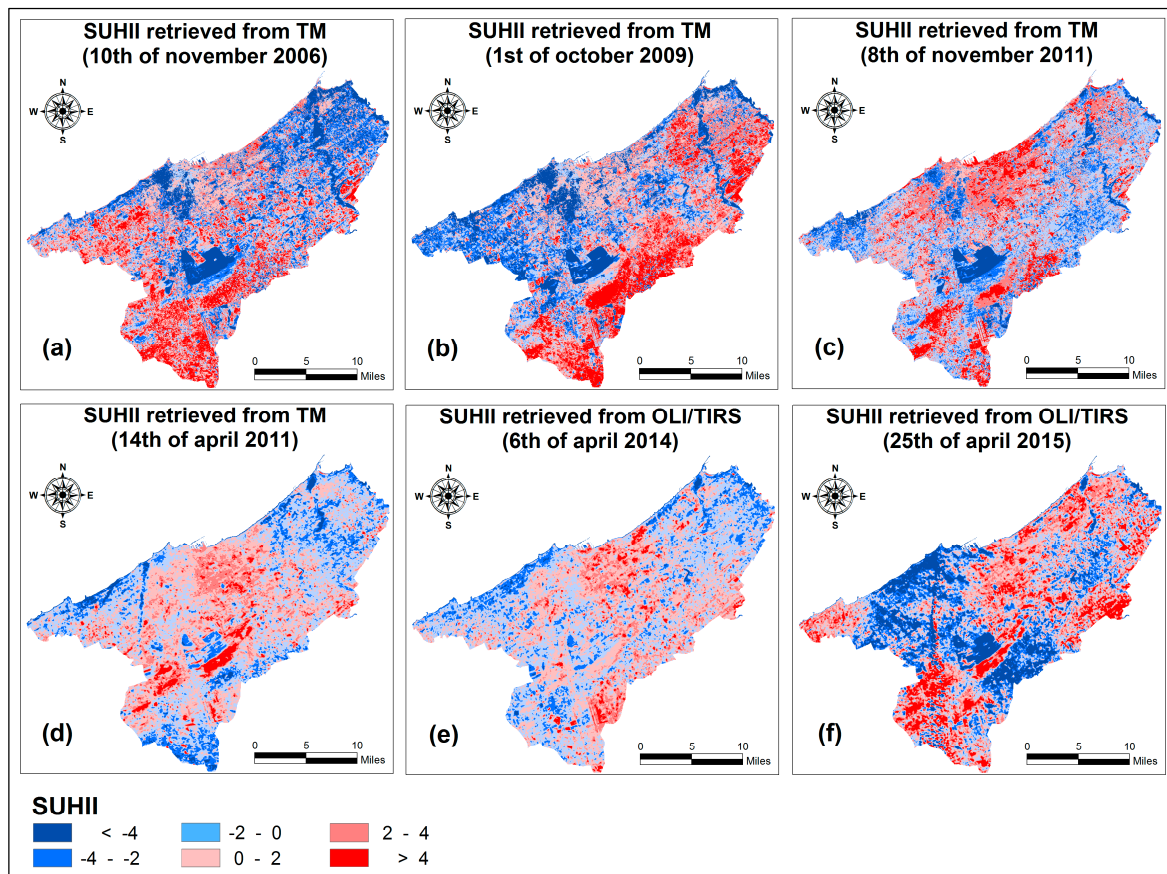


**Figure 14.** Variation of daytime SUHII pattern in autumn and spring period: (a–c) the spatial distribution of SUHII in autumn period between 2006 and 2011; and (d–f) the spatial distribution of SUHII in spring period between 2011 and 2015.

#### 4.6. Variation of Nighttime SUHII

During nighttime, the strength of SUHII in Casablanca region depends on the seasonal variations of urban–rural difference in albedo that controls temperature cooling rate [45,109]. The SUHII reached its maximum in winter of each year coinciding with decreasing LST, while the minimum SUHII is marked during the summer when the LST reaches its peak. Figure 15 shows the variation of LST and SUHII computed based on the eight-day mean MODIS LST product (MOD11A2).

The results also show that the average annual nighttime SUHII between 2005 and 2015 within the commercial cities were constantly at  $2.615 \pm 0.225^{\circ}\text{C}$  and  $2.375 \pm 0.255^{\circ}\text{C}$  for Casablanca and Mohammedia, respectively.

The SUHII is always higher in the urban areas irrespective of the season. Therefore, urban canyons are considered main driver enhancing nighttime SUHII (Figure 16).

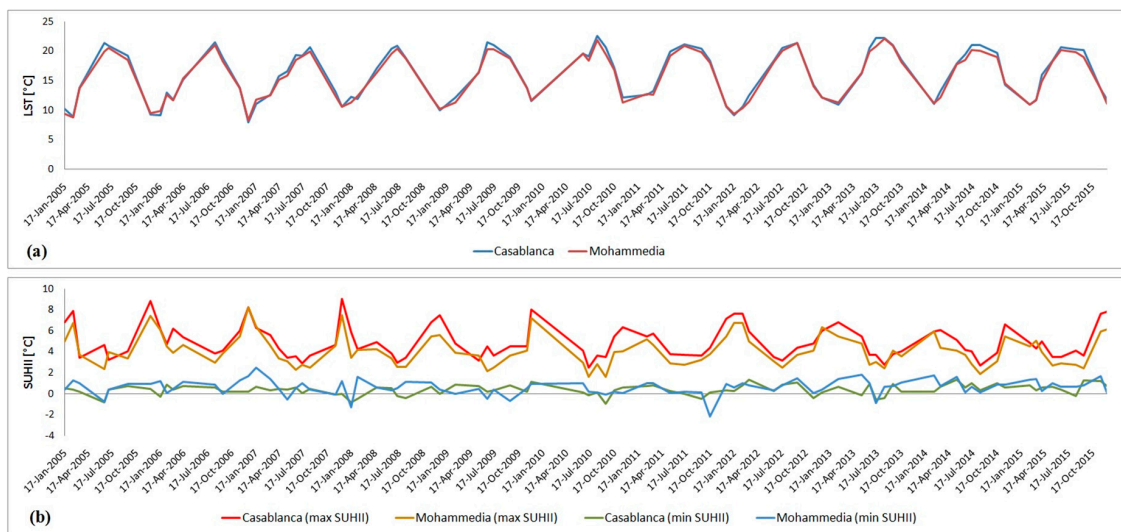


**Figure 15.** (a) Variation of average nighttime LST in Casablanca and Mohammedia between 2005 and 2015 (extracted from MOD11A2 data); and (b) variation of maximum and minimum nighttime SUHII in Casablanca and Mohammedia between 2005 and 2015 (evaluated from MOD11A2 data).

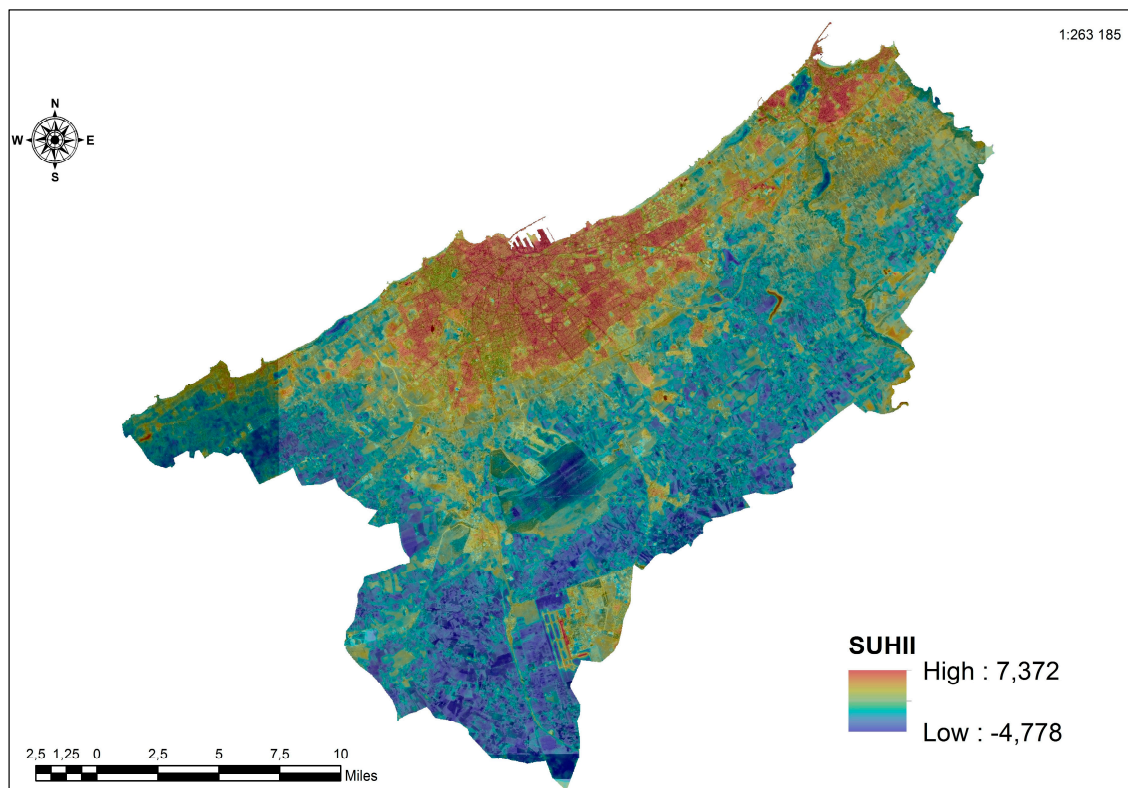


**Figure 16.** Spatial distribution of nighttime SUHII retrieved from OLI/TIRS on 17 June 2015 at 22:22.

## 5. Discussions

### 5.1. Climate Conditions Effect

This research involves the investigation of spatiotemporal variation of SUHII in Casablanca region which is characterized by complex zonal variations. Different drivers highlight the variation

of SUHII such as vegetation [8,110], albedo [111,112], built-up intensity [8,110], anthropogenic heat emissions [46] and city size [9,39,113].

Results show that spatial distribution of SUHII varies considerably during the year and is more pronounced in winter than summer and intermediate seasons. However, in winter some days can escape from this role and show negative SUHII (SUCII) in some areas in the urban core due to the climatic condition and meteorological forcing. Therefore, climate play key role in controlling the SUHII in winter [45] and contributes in regulating albedo [114], and anthropogenic heat emissions [115]. The presence of high air temperature in winter lead to soil moisture deficit [116], which decrease more rapidly in urban areas than the rural through evapotranspiration, and then in enhancing the emergence of SUHII (Figure 5a–c), whereas low temperature keeps, as long as possible, soil moisture high allowing to give the same results in reducing SUHII and UHII as that of vegetation cover (Figure 5d) [45,117]. Moreover, precipitation contributes in increasing soil moisture [47] and then in controlling SUHII [45]. Another study showed that the largest winter UHI follow long periods without precipitation and became much smaller after rain or fog [118].

As regards climate of Casablanca region, the mean annual air temperature is high in the center and east parts of Casablanca city and relatively weakens in the western part [50]. Therefore, it can be observed variations in the spatial distribution of UHI which reaches its maximum in the central part of urban areas especially in winter [10]. At the level of rainfall, the spatial distribution of mean annual precipitation in Casablanca region shows distinctive intensities. The highest values are marked in the northeast of Casablanca region, while the southern areas are driest (Figure 17b) [50]. These spatial variations of precipitation and temperature in Casablanca region contribute significantly in variation of soil moisture and then variation in SUHII pattern.

Figure 17a shows the spatial distribution of SUHII in 6 January 2016 after antecedent precipitation, which reaches 23 mm in the day before image acquisition date (5 January 2016), while Figure 17b represents the mean annual precipitation and wind field (10 m above ground) in Casablanca region extracted from the domains of the Northwest Africa Reanalysis (NwAR) averaged over the first ten hydrological years of the 21st century [50].

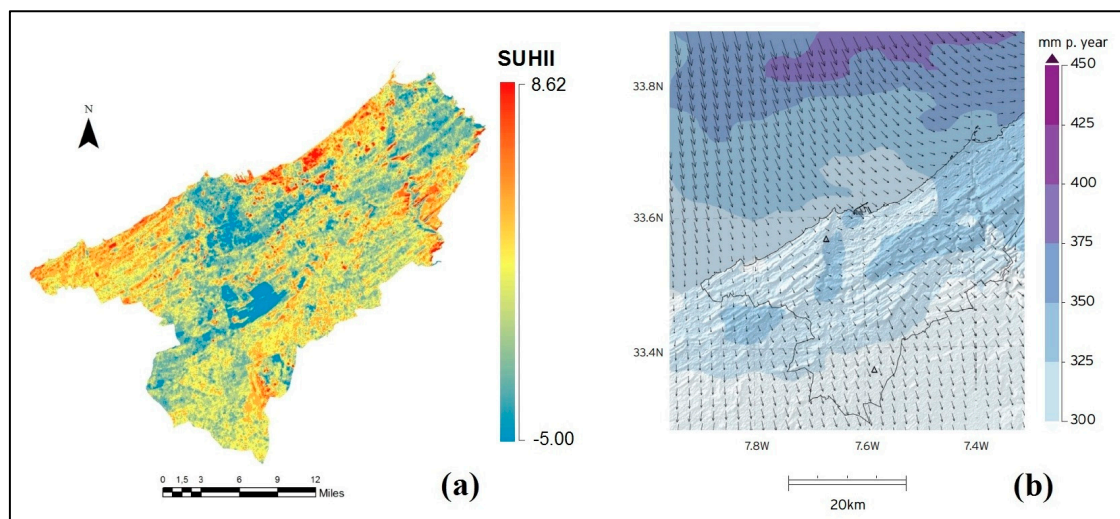


**Figure 17.** (a) Spatial distribution of SUHII in the 6 January 2016 evaluated from Landsat 8; and (b) mean annual of precipitation in the Casablanca region extracted from the domains of the NwAR (source: Urban Agriculture for Growing City Regions [50]).

Figure 17 shows concordance between the spatial distribution of mean annual precipitation and SUHII pattern. Indeed, we observe negative winter SUHII (SUCII) in the areas coinciding with the highest precipitation intensities as the case of the northeast and important parts of the cities in

Casablanca region. The permeable cover in urban areas experienced significant precipitation allows infiltration of rainwater and then occurrence of important soil moisture rate compared to the relatively driest zones of our study area.

The presence of surface heat island in some of rural areas is due to the dry period before precipitation since only 1 mm of precipitation is marked in Casablanca region between the 1 December 2015 and the 4 January 2016, while we observe an important winter air temperature during the same period with mean minimum temperature of 11.2 °C and mean maximum temperature of 22.4 °C. Indeed, the precipitation following a drier period allows increasing of thermal admittance of the most permeable rural areas [118] and contributes significantly in producing surface rural heat islands.

The industrial areas of Casablanca region remain affected by Significant SUHII regardless of the season and climate conditions. While the forests remain the coolest zone, since forest cover holds more soil moisture than other land cover types and exhibited the smallest rate of soil moisture deficit at the annual scale [47].

On the other hand, Climate conditions affect also UHI [119,120] which is significantly correlated with SUHI and specially in the urban areas [19] and in nighttime [20]. They [121] highlighted that LST pixel value coinciding with the weather station location generally indicated a closer relationship to the respective air temperature. This correlation relatively decrease with increasing area covered to compute the mean LST but remain statistically significant ( $p < 0.01$ ) [121].

## 5.2. Comparative Studies

This study shows that the spatial distribution of SUHII is weakest in summer, moderate during spring and autumn, and strongest in winter. Therefore, the regional climate plays a key role in controlling the seasonal cycle of heating and cooling of buildings [122].

These results are similar to some of recent studies that accentuate these statements and which prove the same distribution of UHII, during winter and summer, in some of Japan's cities (Sendai and Tokyo) [48,123,124]. Some recent studies focused on examining the spatiotemporal trend of SUHII in 32 cities across different regions of China, showing that SUHII increases more rapidly in summer than in winter [125]. The same study shows also that both daytime and nighttime SUHII increased dramatically due to the urban development of cities [125].

Another study demonstrates that the UHIs in mid-latitude regions are generally stronger in summer [126] and become more intense near the center of some cities during summer nighttime such as London [126] and Łódź [127].

The SUHII in our study area can be highly variable and complex and it is different from Mediterranean cities [128]. Indeed, a study focused on the evaluation of SUHI in 25 cities around the Mediterranean, from 2001 to 2012, shows that the Southern European cities are affected by positive SUHII, While negative SUHII dominate the Mediterranean cities in Northern Africa [128]. On the other hand, UHI in European Mediterranean cities remain in the most cases influenced by urbanization factor such as the Greater Athens Area [129] and Thessaloniki [130], and is associated to the poor air quality and unfavorable comfort conditions [131].

At the global level, research showed that 36% of cities were affected by significant nocturnal SUHII, especially in the west and south of Asia and northern Africa, while annual daytime and nighttime SUHII are not correlated [46].

## 6. Conclusions

The spatial and temporal variations of the SUHII of the Casablanca region were analyzed. Time series of Landsat TM/ETM+/OLI-TIRS and nightly MODIS data spread over a period of 32 years (from 1984 to 2016) were used. Results show significant SUHII shifts across seasons. Throughout the year, the urban zone of our study area was more conductive to the daytime SUHII in winter and intermediate seasons than in summer. The diurnal SUHII reached the maximum during the winter and spread in a spectacular manner within slum zones, high urban concentration areas, and industrial

areas where important contaminated air is being emitted. However, in winter, SUHII can decrease significantly due to the climate conditions. This research also shows that the urban development encroaching over farmland and green spaces promotes the emergence and the aggravation of the winter SUHII phenomenon. During the summer periods, the spatial distribution of SUHII undergoes reciprocal effect with presence of surface cool islands in the urban areas and a significant warming in the rural surfaces around cities. Surface urban cool island areas appear during the summer because of extended shading in urban canyons and cooling effect of sea breeze in the coastal area. Moreover, the surface heat island intensity becomes relatively moderate in autumn and spring periods. The nocturnal MODIS observations allowed evaluating the variation of nighttime SUHII pattern. The urban core contributes significantly in raising nighttime SUHII while the rural area remains affected by cooling zones. SUHII experiences dramatic change during the year with increasing of this magnitude in winter and significant decrease in summer.

However, the different factors enhancing SUHII/UHII deserve more in depth investigation to understand why the seasonal cycles of SUHII/UHII differs from one city to another. Thus, only combined climatological and remote sensing data would contribute to a better understanding of this phenomenon.

**Acknowledgments:** The authors thank Henri Rueff from Basel University for his invaluable assistance in the proofreading and linguistic revision. We would also like to show our grateful thanks to the editor and anonymous reviewers for their vigilant review of our manuscript.

**Author Contributions:** H.B. Collected, prepared, processed and analyzed data, interpreted and discussed the results, and wrote the manuscript; H.R. Proposed the research concept and contributed in the results interpretation and manuscript editing; A.B. supervised all the work that has been done by the first author; U.F. and D.S Supplied climatological data and contributed with suggestions and comments before submission. All authors reviewed the manuscript.

**Conflicts of Interest:** The authors declare that there is no conflict of interest.

## References

1. United Nations Population Division—Department of Economic and Social Affairs. Available online: <http://www.un.org/en/development/desa/population> (accessed on 5 January 2016).
2. Collier, C.G. The impact of urban areas on weather. *Q. J. R. Meteorol. Soc.* **2006**, *132*, 1–25. [[CrossRef](#)]
3. Taha, H. Urban climates and heat islands: Albedo, evapotranspiration, and anthropogenic heat. *Energy Build.* **1997**, *25*, 99–103. [[CrossRef](#)]
4. Boukhabl, M.; Alkam, D. Impact of vegetation on thermal conditions outside, thermal modeling of urban microclimate, case study: The Street of the Republic, Biskra. *Energy Procedia* **2012**, *18*, 73–84. [[CrossRef](#)]
5. Goodin, D.G.; Harrington, J.A.; Rundquist, B.C. Land cover change and associated trends in surface reflectivity and vegetation index in Southwest Kansas: 1972–1992. *Geocarto Int.* **2002**, *17*, 45–52. [[CrossRef](#)]
6. Cui, L.; Shi, J. Urbanization and its environmental effects in Shanghai, China. *Urban Clim.* **2012**, *2*, 1–15. [[CrossRef](#)]
7. Zhang, Z.; Ji, M.; Shu, J.; Deng, Z.; Wu, Y. Surface urban heat island in Shanghai, China: Examining the relationship between land surface temperature and impervious surface fractions derived from Landsat ETM+ imagery. *Int. Arch. Photogramm. Remote Sens. Spat. Inf. Sci.* **2008**, *37*, 601–606.
8. Tran, H.; Uchihama, D.; Ochi, S.; Yasuoka, Y. Assessment with satellite data of the urban heat island effects in Asian mega cities. *Int. J. Appl. Earth Obs. Geoinf.* **2006**, *8*, 34–48. [[CrossRef](#)]
9. Streutker, D.R. A remote sensing study of the urban heat island of Houston, Texas. *Int. J. Remote Sens.* **2002**, *23*, 2595–2608. [[CrossRef](#)]
10. Rhinane, H.; Hilali, A.; Bahi, H.; Berrada, A. Contribution of Landsat TM Data for the detection of urban heat islands areas case of Casablanca. *J. Geogr. Inf. Syst.* **2012**, *4*, 20–26.
11. Sakhy, A.; Madelin, M.; Beltrando, G. Les échelles d'étude de l'îlot de chaleur urbain et ses relations avec la végétation et la géométrie de la ville (exemple de Paris). In Proceedings of the Dixièmes Rencontres de Théo Quant, Paris, France, 23–25 February 2011.

12. Tan, J.; Zheng, Y.; Tang, X.; Guo, C.; Li, L.; Song, G.; Zhen, X.; Yuan, D.; Kalkstein, A.J.; Li, F.; et al. The urban heat island and its impact on heat waves and human health in Shanghai. *Int. J. Biometeorol.* **2010**, *54*, 75–84. [[CrossRef](#)] [[PubMed](#)]
13. Gong, P.; Liang, S.; Carlton, E.J.; Jiang, Q.; Wu, J.; Wang, L.; Remais, J.V. Urbanisation and health in China. *Lancet* **2012**, *379*, 843–852. [[CrossRef](#)]
14. Muthers, S.; Matzarakis, A.; Koch, E. Summer climate and mortality in Vienna—A human-biometeorological approach of heat-related mortality during the heat waves in 2003. *Wien. Klin. Wochenschr.* **2010**, *122*, 525–531. [[CrossRef](#)] [[PubMed](#)]
15. O'Loughlin, J.; Witmer, F.D.W.; Linke, A.M.; Laing, A.; Gettelman, A.; Dudhia, J. Climate variability and conflict risk in East Africa, 1990–2009. *Proc. Natl. Acad. Sci. USA* **2012**, *109*, 18344–18349. [[CrossRef](#)] [[PubMed](#)]
16. Patz, J.A.; Campbell-Lendrum, D.; Holloway, T.; Foley, J.A. Impact of regional climate change on human health. *Nature* **2005**, *438*, 310–317. [[CrossRef](#)] [[PubMed](#)]
17. Oke, T.R. The heat island of the urban boundary layer: Characteristics, causes and effects. In *Wind Climate in Cities*; Cermak, J.E., Davenport, A.G., Plate, E.J., Viegas, D.X., Eds.; Springer: Dordrecht, The Netherlands, 1995; pp. 81–107.
18. Saaroni, H.; Ben-Dor, E.; Bitan, A.; Potchter, O. Spatial distribution and microscale characteristics of the urban heat island in Tel-Aviv, Israel. *Landsc. Urban Plan.* **2000**, *48*, 1–18. [[CrossRef](#)]
19. Schwarz, N.; Lautenbach, S.; Seppelt, R. Exploring indicators for quantifying surface urban heat islands of European cities with MODIS land surface temperatures. *Remote Sens. Environ.* **2011**, *115*, 3175–3186. [[CrossRef](#)]
20. Voogt, J.; Oke, T. Thermal remote sensing of urban climates. *Remote Sens. Environ.* **2003**, *86*, 370–384. [[CrossRef](#)]
21. Bektaş Balçık, F. Determining the impact of urban components on land surface temperature of Istanbul by using remote sensing indices. *Environ. Monit. Assess.* **2014**, *186*, 859–872. [[CrossRef](#)] [[PubMed](#)]
22. Weng, Q. Thermal infrared remote sensing for urban climate and environmental studies: Methods, applications, and trends. *ISPRS J. Photogramm. Remote Sens.* **2009**, *64*, 335–344. [[CrossRef](#)]
23. Dihkan, M.; Karsli, F.; Guneroglu, A.; Guneroglu, N. Evaluation of surface urban heat island (SUHI) effect on coastal zone: The case of Istanbul Megacity. *Ocean Coast. Manag.* **2015**, *118*, 309–316. [[CrossRef](#)]
24. Li, Y.; Zhang, H.; Kainz, W. Monitoring patterns of urban heat islands of the fast-growing Shanghai metropolis, China: Using time-series of Landsat TM/ETM+ data. *Int. J. Appl. Earth Obs. Geoinf.* **2012**, *19*, 127–138. [[CrossRef](#)]
25. Wang, K.; Wang, J.; Wang, P.; Sparrow, M.; Yang, J.; Chen, H. Influences of urbanization on surface characteristics as derived from the moderate-resolution imaging spectroradiometer: A case study for the Beijing metropolitan area. *J. Geophys. Res.* **2007**. [[CrossRef](#)]
26. Frey, C.M.; Kuenzer, C.; Dech, S. Quantitative comparison of the operational NOAA-AVHRR LST product of DLR and the MODIS LST product V005. *Int. J. Remote Sens.* **2012**, *33*, 7165–7183. [[CrossRef](#)]
27. Mao, K.; Qin, Z.; Shi, J.; Gong, P. A practical split-window algorithm for retrieving land-surface temperature from MODIS data. *Int. J. Remote Sens.* **2005**, *26*, 3181–3204. [[CrossRef](#)]
28. Kato, S.; Yamaguchi, Y. Analysis of urban heat-island effect using ASTER and ETM+ Data: Separation of anthropogenic heat discharge and natural heat radiation from sensible heat flux. *Remote Sens. Environ.* **2005**, *99*, 44–54. [[CrossRef](#)]
29. Lu, D.; Weng, Q. Spectral mixture analysis of ASTER images for examining the relationship between urban thermal features and biophysical descriptors in Indianapolis, Indiana, USA. *Remote Sens. Environ.* **2006**, *104*, 157–167. [[CrossRef](#)]
30. Liu, H.; Weng, Q. Seasonal variations in the relationship between landscape pattern and land surface temperature in Indianapolis, USA. *Environ. Monit. Assess.* **2008**, *144*, 199–219. [[CrossRef](#)] [[PubMed](#)]
31. Weng, Q.; Lu, D.; Schubring, J. Estimation of land surface temperature—Vegetation abundance relationship for urban heat island studies. *Remote Sens. Environ.* **2004**, *89*, 467–483. [[CrossRef](#)]
32. Yue, W.; Xu, J.; Tan, W.; Xu, L. The relationship between land surface temperature and NDVI with remote sensing: Application to Shanghai Landsat 7 ETM+ data. *Int. J. Remote Sens.* **2007**, *28*, 3205–3226. [[CrossRef](#)]
33. Xiao, R.; Weng, Q.; Ouyang, Z.; Li, W.; Schienke, E.W.; Zhang, Z. Land surface temperature variation and major factors in Beijing, China. *Photogramm. Eng. Remote Sens.* **2008**, *74*, 451–461. [[CrossRef](#)]

34. Elvidge, C.D.; Baugh, K.E.; Kihn, E.A.; Kroehl, H.W.; Davis, E.R.; Davis, C.W. Relation between satellite observed visible-near infrared emissions, population, economic activity and electric power consumption. *Int. J. Remote Sens.* **1997**, *18*, 1373–1379. [[CrossRef](#)]
35. Ghobadi, Y.; Pradhan, B.; Shafri, H.Z.M.; Kabiri, K. Assessment of spatial relationship between land surface temperature and land use/cover retrieval from multi-temporal remote sensing data in South Karkheh Sub-basin, Iran. *Arab. J. Geosci.* **2015**, *8*, 525–537. [[CrossRef](#)]
36. Tan, K.C.; Lim, H.S.; Mat Jafri, M.Z.; Abdullah, K. A comparison of radiometric correction techniques in the evaluation of the relationship between LST and NDVI in Landsat imagery. *Environ. Monit. Assess.* **2012**, *184*, 3813–3829. [[CrossRef](#)] [[PubMed](#)]
37. Gallo, K.P.; Tarpley, J.D.; McNab, A.L.; Karl, T.R. Assessment of urban heat islands: A satellite perspective. *Atmos. Res.* **1995**, *37*, 37–43. [[CrossRef](#)]
38. Nie, Q.; Xu, J. Understanding the effects of the impervious surfaces pattern on land surface temperature in an urban area. *Front. Earth Sci.* **2015**, *9*, 276–285. [[CrossRef](#)]
39. Imhoff, M.L.; Zhang, P.; Wolfe, R.E.; Bounoua, L. Remote sensing of the urban heat island effect across biomes in the continental USA. *Remote Sens. Environ.* **2010**, *114*, 504–513. [[CrossRef](#)]
40. Stathopoulou, M.; Cartalis, C. Daytime urban heat islands from Landsat ETM+ and Corine land cover data: An application to major cities in Greece. *Sol. Energy* **2007**, *81*, 358–368. [[CrossRef](#)]
41. Dousset, B.; Gourmelon, F.; Laaidi, K.; Zeghnoun, A.; Giraudet, E.; Bretin, P.; Mauri, E.; Vandentorren, S. Satellite monitoring of summer heat waves in the Paris metropolitan area. *Int. J. Climatol.* **2011**, *31*, 313–323. [[CrossRef](#)]
42. Hu, Y.; Jia, G. Influence of land use change on urban heat island derived from multi-sensor data. *Int. J. Climatol.* **2009**. [[CrossRef](#)]
43. Clinton, N.; Gong, P. MODIS detected surface urban heat islands and sinks: Global locations and controls. *Remote Sens. Environ.* **2013**, *134*, 294–304. [[CrossRef](#)]
44. Ichinose, T.; Shimodozo, K.; Hanaki, K. Impact of anthropogenic heat on urban climate in Tokyo. *Atmos. Environ.* **1999**, *33*, 3897–3909. [[CrossRef](#)]
45. Zhou, D.; Zhao, S.; Liu, S.; Zhang, L.; Zhu, C. Surface urban heat island in China's 32 major cities: Spatial patterns and drivers. *Remote Sens. Environ.* **2014**, *152*, 51–61. [[CrossRef](#)]
46. Peng, S.; Piao, S.; Ciais, P.; Friedlingstein, P.; Ottle, C.; Bréon, F.-M.; Nan, H.; Zhou, L.; Myneni, R.B. Surface urban heat island across 419 global big cities. *Environ. Sci. Technol.* **2012**, *46*, 696–703. [[CrossRef](#)] [[PubMed](#)]
47. Feng, H.; Liu, Y. Combined effects of precipitation and air temperature on soil moisture in different land covers in a humid basin. *J. Hydrol.* **2015**, *531*, 1129–1140. [[CrossRef](#)]
48. Sakaida, K.; Egoshi, A.; Kuramochi, M. Effects of sea breezes on mitigating urban heat island phenomenon: Vertical observation results in the urban center of Sendai. *J. Geogr.* **2011**, *120*, 382–391. [[CrossRef](#)]
49. Moulali, T. *L'émigration Internationale et le Problème du Retour à Casablanca*; Université des Sciences et Technologies: Lille, France, 1992.
50. Giseke, U.; Gerster-Bentaya, M.; Helten, F.; Kraume, M.; Scherer, D.; Spars, G.; Amraoui, F.; Adidi, A.; Berdouz, S.; Chlaida, M.; et al. *Urban Agriculture for Growing City Regions: Connecting Urban-Rural Spheres in Casablanca*; Routledge: Abingdon, VI, USA, 2015.
51. Roy, D.P.; Wulder, M.A.; Loveland, T.R.; Woodcock, C.E.; Allen, R.G.; Anderson, M.C.; Helder, D.; Irons, J.R.; Johnson, D.M.; Kennedy, R.; et al. Landsat-8: Science and product vision for terrestrial global change research. *Remote Sens. Environ.* **2014**, *145*, 154–172. [[CrossRef](#)]
52. Irons, J.R.; Dwyer, J.L.; Barsi, J.A. The next Landsat satellite: The Landsat data continuity mission. *Remote Sens. Environ.* **2012**, *122*, 11–21. [[CrossRef](#)]
53. Chander, G.; Markham, B.L.; Barsi, J.A. Revised Landsat-5 Thematic Mapper Radiometric calibration. *IEEE Geosci. Remote Sens. Lett.* **2007**, *4*, 490–494. [[CrossRef](#)]
54. Markham, B.; Barsi, J.; Kvaran, G.; Ong, L.; Kaita, E.; Biggar, S.; Czapla-Myers, J.; Mishra, N.; Helder, D. Landsat-8 operational land imager radiometric calibration and stability. *Remote Sens.* **2014**, *6*, 12275–12308. [[CrossRef](#)]
55. Czapla-Myers, J.; McCorkel, J.; Anderson, N.; Thome, K.; Biggar, S.; Helder, D.; Aaron, D.; Leigh, L.; Mishra, N. The ground-based absolute radiometric calibration of Landsat 8 OLI. *Remote Sens.* **2015**, *7*, 600–626. [[CrossRef](#)]

56. Chander, G.; Markham, B.L.; Helder, D.L. Summary of current radiometric calibration coefficients for Landsat MSS, TM, ETM+, and EO-1 ALI sensors. *Remote Sens. Environ.* **2009**, *113*, 893–903. [[CrossRef](#)]
57. Chen, D.; Brutsaert, W. Satellite-Sensed Distribution and Spatial Patterns of Vegetation Parameters over a Tallgrass Prairie. *J. Atmos. Sci.* **1998**, *55*, 1225–1238. [[CrossRef](#)]
58. Yuvaraj, E.; Dharañirajan, K.; Saravanan, N.K. Evaluation of Vegetation density of the Mangrove forest in South Andaman Island using Remote Sensing and GIS techniques. *Int. Res. J. Environ. Sci.* **2014**, *3*, 19–25.
59. Verrelst, J.; Romijn, E.; Kooistra, L. Mapping vegetation density in a heterogeneous river floodplain ecosystem using pointable CHRIS/PROBA data. *Remote Sens.* **2012**, *4*, 2866–2889. [[CrossRef](#)]
60. Bunn, A.G.; Goetz, S.J. Trends in Satellite-observed circumpolar photosynthetic activity from 1982 to 2003: The influence of seasonality, cover type, and vegetation density. *Earth Interact.* **2006**, *10*, 1–19. [[CrossRef](#)]
61. Tucker, C.J. Red and photographic infrared linear combinations for monitoring vegetation. *Remote Sens. Environ.* **1979**, *8*, 127–150. [[CrossRef](#)]
62. Bannari, A.; Teillet, P.M.; Landry, R. Comparaison des réflectances de surfaces naturelles dans les bandes spectrales homologues des capteurs TM de Landsat-5 ET ETM+ de Landsat-7. *Télédétection* **2004**, *4*, 263–275.
63. Roy, D.P.; Kovalevskyy, V.; Zhang, H.K.; Vermote, E.F.; Yan, L.; Kumar, S.S.; Egorov, A. Characterization of Landsat-7 to Landsat-8 reflective wavelength and normalized difference vegetation index continuity. *Remote Sens. Environ.* **2016**. [[CrossRef](#)]
64. Mishra, N.; Haque, M.; Leigh, L.; Aaron, D.; Helder, D.; Markham, B. Radiometric cross calibration of Landsat 8 Operational Land Imager (OLI) and Landsat 7 Enhanced Thematic Mapper Plus (ETM+). *Remote Sens.* **2014**, *6*, 12619–12638. [[CrossRef](#)]
65. Teillet, P.; Barker, J.; Markham, B.; Irish, R.; Fedosejevs, G.; Storey, J. Radiometric cross-calibration of the Landsat-7 ETM+ and Landsat-5 TM sensors based on tandem data sets. *Remote Sens. Environ.* **2001**, *78*, 39–54. [[CrossRef](#)]
66. Figoski, J.W.; Zaun, N.; Mooney, T. Performance results for the Landsat OLI spectral filters. *Proc. SPIE* **2009**. [[CrossRef](#)]
67. Li, P.; Jiang, L.; Feng, Z. Cross-comparison of vegetation indices derived from Landsat-7 Enhanced Thematic Mapper Plus (ETM+) and Landsat-8 Operational Land Imager (OLI) sensors. *Remote Sens.* **2013**, *6*, 310–329. [[CrossRef](#)]
68. Barsi, J.; Lee, K.; Kvaran, G.; Markham, B.; Pedelty, J. The spectral response of the Landsat-8 operational land imager. *Remote Sens.* **2014**, *6*, 10232–10251. [[CrossRef](#)]
69. Valor, E. Mapping land surface emissivity from NDVI: Application to European, African, and South American areas. *Remote Sens. Environ.* **1996**, *57*, 167–184. [[CrossRef](#)]
70. Li, X.; Li, W.; Middel, A.; Harlan, S.L.; Brazel, A.J.; Turner, B.L. Remote sensing of the surface urban heat island and land architecture in Phoenix, Arizona: Combined effects of land composition and configuration and cadastral demographic—Economic factors. *Remote Sens. Environ.* **2016**, *174*, 233–243. [[CrossRef](#)]
71. Sobrino, J.A.; Jimenez-Muoz, J.C.; Soria, G.; Romaguera, M.; Guanter, L.; Moreno, J.; Plaza, A.; Martinez, P. Land Surface Emissivity Retrieval From Different VNIR and TIR Sensors. *IEEE Trans. Geosci. Remote Sens.* **2008**, *46*, 316–327. [[CrossRef](#)]
72. Yu, X.; Guo, X.; Wu, Z. Land surface temperature retrieval from Landsat 8 TIRS—Comparison between radiative transfer equation-based method, split window algorithm and single channel method. *Remote Sens.* **2014**, *6*, 9829–9852. [[CrossRef](#)]
73. Sobrino, J.A.; Raissouni, N. Toward remote sensing methods for land cover dynamic monitoring: Application to Morocco. *Int. J. Remote Sens.* **2000**, *21*, 353–366. [[CrossRef](#)]
74. Carlson, T.N.; Ripley, D.A. On the relation between NDVI, fractional vegetation cover, and leaf area index. *Remote Sens. Environ.* **1997**, *62*, 241–252. [[CrossRef](#)]
75. Allen, R.G.; Tasumi, M.; Morse, A.; Trezza, R.; Wright, J.L.; Bastiaanssen, W.; Kramber, W.; Lorite, I.; Robison, C.W. Satellite-Based energy balance for Mapping Evapotranspiration with Internalized Calibration (METRIC)—Applications. *J. Irrig. Drain. Eng.* **2007**, *133*, 395–406. [[CrossRef](#)]
76. Anderson, M.C.; Norman, J.M.; Mecikalski, J.R.; Otkin, J.A.; Kustas, W.P. A climatological study of evapotranspiration and moisture stress across the continental United States based on thermal remote sensing: 1. Model formulation. *J. Geophys. Res.* **2007**. [[CrossRef](#)]
77. Bechtel, B.; Zakšek, K.; Hoshyaripour, G. Downscaling land surface temperature in an urban area: A Case study for Hamburg, Germany. *Remote Sens.* **2012**, *4*, 3184–3200. [[CrossRef](#)]

78. Zakšek, K.; Oštir, K. Downscaling land surface temperature for urban heat island diurnal cycle analysis. *Remote Sens. Environ.* **2012**, *117*, 114–124. [[CrossRef](#)]
79. Ayanlade, A.; Jegede, O.O. Evaluation of the intensity of the daytime surface urban heat island: How can remote sensing help? *Int. J. Image Data Fusion* **2015**, *6*, 348–365. [[CrossRef](#)]
80. Qin, Z.; Karnieli, A.; Berliner, P. A mono-window algorithm for retrieving land surface temperature from Landsat TM data and its application to the Israel-Egypt border region. *Int. J. Remote Sens.* **2001**, *22*, 3719–3746. [[CrossRef](#)]
81. Jiménez-Muñoz, J.C. A generalized single-channel method for retrieving land surface temperature from remote sensing data. *J. Geophys. Res.* **2003**. [[CrossRef](#)]
82. Sobrino, J.A.; Caselles, V.; Coll, C. Theoretical split-window algorithms for determining the actual surface temperature. *IL Nuovo Cimento* **1993**, *16*, 219–236. [[CrossRef](#)]
83. Becker, F.; Li, Z.L. Towards a local split window method over land surfaces. *Int. J. Remote Sens.* **1990**, *11*, 369–393. [[CrossRef](#)]
84. Sobrino, J.A.; Sòria, G.; Prata, A.J. Surface temperature retrieval from Along Track Scanning Radiometer 2 data: Algorithms and validation. *J. Geophys. Res.* **2004**. [[CrossRef](#)]
85. Chedin, A.; Scott, N.A.; Berroir, A. A Single-Channel, double-viewing angle method for sea surface temperature determination from coincident METEOSAT and TIROS-N radiometric measurements. *J. Appl. Meteorol.* **1982**, *21*, 613–618. [[CrossRef](#)]
86. Prata, A.J. Land surface temperatures derived from the advanced very high resolution radiometer and the along-track scanning radiometer: 1. Theory. *J. Geophys. Res.* **1993**. [[CrossRef](#)]
87. Zhaoliang, L.; Stoll, M.P.; Renhua, Z.; Li, J.; Zhongbo, S. On the separate retrieval of soil and vegetation temperatures from ATSR data. *Sci. Chin. Ser. Earth Sci.* **2001**, *44*, 97–111. [[CrossRef](#)]
88. Artis, D.A.; Carnahan, W.H. Survey of emissivity variability in thermography of urban areas. *Remote Sens. Environ.* **1982**, *12*, 313–329. [[CrossRef](#)]
89. Sobrino, J.; Coll, C.; Caselles, V. Atmospheric correction for land surface temperature using NOAA-11 AVHRR channels 4 and 5. *Remote Sens. Environ.* **1991**, *38*, 19–34. [[CrossRef](#)]
90. Du, C.; Ren, H.; Qin, Q.; Meng, J.; Zhao, S. A Practical split-window algorithm for estimating land surface temperature from Landsat 8 data. *Remote Sens.* **2015**, *7*, 647–665. [[CrossRef](#)]
91. Zha, Y.; Gao, J.; Ni, S. Use of normalized difference built-up index in automatically mapping urban areas from TM imagery. *Int. J. Remote Sens.* **2003**, *24*, 583–594. [[CrossRef](#)]
92. Xu, H. A new index for delineating built-up land features in satellite imagery. *Int. J. Remote Sens.* **2008**, *29*, 4269–4276. [[CrossRef](#)]
93. Holsten, A.; Vetter, T.; Vohland, K.; Krysanova, V. Impact of climate change on soil moisture dynamics in Brandenburg with a focus on nature conservation areas. *Ecol. Model.* **2009**, *220*, 2076–2087. [[CrossRef](#)]
94. Wang, G.; Li, Y.; Hu, H.; Wang, Y. Synergistic effect of vegetation and air temperature changes on soil water content in alpine frost meadow soil in the permafrost region of Qinghai-Tibet. *Hydrol. Process.* **2008**, *22*, 3310–3320. [[CrossRef](#)]
95. Freedman, M.; Jaggi, B. Global warming, commitment to the Kyoto protocol, and accounting disclosures by the largest global public firms from polluting industries. *Int. J. Account.* **2005**, *40*, 215–232. [[CrossRef](#)]
96. Daniel, B.; Stanisstreet, M.; Boyes, E. How can we best reduce global warming? School students' ideas and misconceptions. *Int. J. Environ. Stud.* **2004**, *61*, 211–222. [[CrossRef](#)]
97. Lashof, D.A.; Ahuja, D.R. Relative contributions of greenhouse gas emissions to global warming. *Nature* **1990**, *344*, 529–531. [[CrossRef](#)]
98. Shine, K.P.; Fuglestvedt, J.S.; Hailemariam, K.; Stuber, N. Alternatives to the global warming potential for comparing climate impacts of emissions of greenhouse gases. *Clim. Chang.* **2005**, *68*, 281–302. [[CrossRef](#)]
99. Cartalis, C. Climatic Change in the built environment in temperate climates with emphasis on the Mediterranean Area. In *Energy Performance of Buildings*; Boemi, S.N., Irulegi, O., Santamouris, M., Eds.; Springer International Publishing: Cham, Switzerland, 2016; pp. 19–36.
100. Zhang, J.; Li, Y.; Wang, Y. Monitoring the urban heat island and the spatial expansion: Using thermal remote sensing image of ETM+ band6. *Proc. SPIE* **2007**. [[CrossRef](#)]
101. Abraha, M.G.; Savage, M.J. Potential impacts of climate change on the grain yield of maize for the midlands of KwaZulu-Natal, South Africa. *Agric. Ecosyst. Environ.* **2006**, *115*, 150–160. [[CrossRef](#)]

102. Kang, Y.; Khan, S.; Ma, X. Climate change impacts on crop yield, crop water productivity and food security—A review. *Prog. Nat. Sci.* **2009**, *19*, 1665–1674. [[CrossRef](#)]
103. Patz, J.A.; Gibbs, H.K.; Foley, J.A.; Rogers, J.V.; Smith, K.R. Climate change and global health: Quantifying a growing ethical crisis. *EcoHealth* **2007**, *4*, 397–405. [[CrossRef](#)]
104. Magadza, C.H. Climate Change Impacts and Human Settlements in Africa: Prospects for adaptation. *Environ. Monit. Assess.* **2000**, *61*, 193–205. [[CrossRef](#)]
105. Santamouris, M. Analyzing the heat island magnitude and characteristics in one hundred Asian and Australian cities and regions. *Sci. Total Environ.* **2015**, *512–513*, 582–598. [[CrossRef](#)] [[PubMed](#)]
106. Sashiyama, S.; Yamamoto, K. Method for evaluating the influence of obstruction of Sea Breeze by clusters of high-rise buildings on the urban heat island effect. *J. Environ. Prot.* **2014**, *5*, 983–996. [[CrossRef](#)]
107. Ohashi, Y.; Kida, H. Local Circulations Developed in the vicinity of both coastal and inland urban areas: A numerical study with a mesoscale atmospheric model. *J. Appl. Meteorol.* **2002**, *41*, 30–45. [[CrossRef](#)]
108. Chow, W.T.L.; Roth, M. Temporal dynamics of the urban heat island of Singapore. *Int. J. Climatol.* **2006**, *26*, 2243–2260. [[CrossRef](#)]
109. Quan, J.; Zhan, W.; Chen, Y.; Wang, M.; Wang, J. Time series decomposition of remotely sensed land surface temperature and investigation of trends and seasonal variations in surface urban heat islands: Thermal image series decomposition. *J. Geophys. Res. Atmos.* **2016**, *121*, 2638–2657. [[CrossRef](#)]
110. Yuan, F.; Bauer, M.E. Comparison of impervious surface area and normalized difference vegetation index as indicators of surface urban heat island effects in Landsat imagery. *Remote Sens. Environ.* **2007**, *106*, 375–386. [[CrossRef](#)]
111. Oke, T.R. The energetic basis of the urban heat island. *Q. J. R. Meteorol. Soc.* **1982**, *108*, 1–24. [[CrossRef](#)]
112. Stewart, I.D.; Oke, T.R. Local Climate zones for urban temperature studies. *Bull. Am. Meteorol. Soc.* **2012**, *93*, 1879–1900. [[CrossRef](#)]
113. Nichol, J.E. High-Resolution surface temperature patterns related to urban morphology in a tropical city: A Satellite-based study. *J. Appl. Meteorol.* **1996**, *35*, 135–146. [[CrossRef](#)]
114. Hall, A. The role of surface albedo feedback in climate. *J. Clim.* **2004**, *17*, 1550–1568. [[CrossRef](#)]
115. Santamouris, M.; Papanikolaou, N.; Livada, I.; Koronakis, I.; Georgakis, C.; Argiriou, A.; Assimakopoulos, D. On the impact of urban climate on the energy consumption of buildings. *Sol. Energy* **2001**, *70*, 201–216. [[CrossRef](#)]
116. Lofgren, B.M.; Hunter, T.S.; Wilbarger, J. Effects of using air temperature as a proxy for potential evapotranspiration in climate change scenarios of Great Lakes basin hydrology. *J. Gt. Lakes Res.* **2011**, *37*, 744–752. [[CrossRef](#)]
117. Lakshmi, V.; Zehrfuhs, D.; Jackson, T. Observations of land surface temperature and its relationship to soil moisture during SGP99. In Proceedings of the IEEE 2000 International Geoscience and Remote Sensing Symposium, Honolulu, HI, USA, 24–28 July 2000; pp. 1256–1258.
118. Runnalls, K.E.; Oke, T.R. Dynamics and controls of the near surface heat island of Vancouver, British Columbia. *Phys. Geogr.* **2000**, *21*, 283–304.
119. Zhao, L.; Lee, X.; Smith, R.B.; Oleson, K. Strong contributions of local background climate to urban heat islands. *Nature* **2014**, *511*, 216–219. [[CrossRef](#)] [[PubMed](#)]
120. Cohen, P.; Potchter, O.; Matzarakis, A. Daily and seasonal climatic conditions of green urban open spaces in the Mediterranean climate and their impact on human comfort. *Build. Environ.* **2012**, *51*, 285–295. [[CrossRef](#)]
121. Schwarz, N.; Schlink, U.; Franck, U.; Großmann, K. Relationship of land surface and air temperatures and its implications for quantifying urban heat island indicators—An application for the city of Leipzig (Germany). *Ecol. Indic.* **2012**, *18*, 693–704. [[CrossRef](#)]
122. Jauregui, E.; Godinez, L.; Cruz, F. Aspects of heat-island development in Guadalajara, Mexico. *Atmos. Environ. Part B Urban Atmos.* **1992**, *26*, 391–396. [[CrossRef](#)]
123. Sakaida, K.; Egoshi, A. *Influences of Sea Breeze on Urban Heat Island in Sendai, Japan*; Inspiro AB: Göteborg, Sweden, 2006; pp. 388–391.
124. Tokairin, T.; Kondo, H.; Kikegawa, Y. *Potential of Sea Breeze from The Tokyo Bay for Natural Ventilation in Buildings*; Inspiro AB: Göteborg, Sweden, 2006; pp. 525–527.
125. Zhou, D.; Zhang, L.; Hao, L.; Sun, G.; Liu, Y.; Zhu, C. Spatiotemporal trends of urban heat island effect along the urban development intensity gradient in China. *Sci. Total Environ.* **2016**, *544*, 617–626. [[CrossRef](#)] [[PubMed](#)]

126. Wilby, R.L. Past and projected trends in London's urban heat island. *Weather* **2003**, *58*, 251–260. [[CrossRef](#)]
127. Kłysik, K.; Fortuniak, K. Temporal and spatial characteristics of the urban heat island of Łódź, Poland. *Atmos. Environ.* **1999**, *33*, 3885–3895. [[CrossRef](#)]
128. Benas, N.; Chrysoulakis, N.; Poursanidis, D. The surface urban heat island in large Mediterranean cities during the last decade: Annual characteristics and trends based on EO data. In Proceedings of the Mediterranean City 2014: Adaptation Strategies to Global Environmental Change in the Mediterranean City and the Role of Global Earth Observations, Athens, Greece, 10–11 June 2014.
129. Mihalakakou, G.; Santamouris, M.; Papanikolaou, N.; Cartalis, C.; Tsangrassoulis, A. Simulation of the urban heat island phenomenon in Mediterranean climates. *Pure Appl. Geophys.* **2004**, *161*, 429–451. [[CrossRef](#)]
130. Giannaros, T.M.; Melas, D. Study of the urban heat island in a coastal Mediterranean City: The case study of Thessaloniki, Greece. *Atmos. Res.* **2012**, *118*, 103–120. [[CrossRef](#)]
131. Poupkou, A.; Nastos, P.; Melas, D.; Zerefos, C. Climatology of discomfort index and air quality index in a large urban Mediterranean agglomeration. *Water. Air. Soil Pollut.* **2011**, *222*, 163–183. [[CrossRef](#)]



© 2016 by the authors; licensee MDPI, Basel, Switzerland. This article is an open access article distributed under the terms and conditions of the Creative Commons Attribution (CC-BY) license (<http://creativecommons.org/licenses/by/4.0/>).